

The cause of ‘weak-link’ grain boundary behaviour in polycrystalline $\text{Bi}_2\text{Sr}_2\text{CaCu}_2\text{O}_8$ and $\text{Bi}_2\text{Sr}_2\text{Ca}_2\text{Cu}_3\text{O}_{10}$ superconductors

Guanmei Wang, Mark J Raine and Damian P Hampshire 

Durham University, Department of Physics, Superconductivity Group, South Road, Durham, DH1 3LE, United Kingdom

E-mail: guanmei.wang@durham.ac.uk

Received 2 October 2017, revised 4 December 2017

Accepted for publication 14 December 2017

Published 16 January 2018



Abstract

The detrimental effects of grain boundaries have long been considered responsible for the low critical current densities (J_c) in high temperature superconductors. In this paper, we apply the quantitative approach used to identify the cause of the ‘weak-link’ grain boundary behaviour in $\text{YBa}_2\text{Cu}_3\text{O}_7$ (Wang *et al* 2017 *Supercond. Sci. Technol.* **30** 104001), to the $\text{Bi}_2\text{Sr}_2\text{CaCu}_2\text{O}_8$ and $\text{Bi}_2\text{Sr}_2\text{Ca}_2\text{Cu}_3\text{O}_{10}$ materials that we have fabricated. Magnetic and transport measurements are used to characterise the grain and grain boundary properties of micro- and nanocrystalline materials. Magnetisation measurements on all nanocrystalline materials show non-Bean-like behaviour and are consistent with surface pinning. $\text{Bi}_2\text{Sr}_2\text{CaCu}_2\text{O}_8$: our microcrystalline material has very low grain boundary resistivity (ρ_{GB}), which is similar to that of the grains (ρ_G) such that $\rho_{GB} \approx \rho_G = 2 \times 10^{-5} \Omega\text{m}$ (assuming a grain boundary thickness (d) of 1 nm) equivalent to an areal resistivity of $\rho_G = 2 \times 10^{-14} \Omega\text{m}^2$. The transport J_c values are consistent with well-connected grains and very weak grain boundary pinning. However, unlike low temperature superconductors (LTS) in which decreasing grain size increases the pinning along the grain boundary channels, any increase in pinning produced by making the grains in our $\text{Bi}_2\text{Sr}_2\text{CaCu}_2\text{O}_8$ materials nanocrystalline was completely offset by a decrease in the depairing current density of the grain boundaries caused by their high resistivity. We suggest a different approach to increasing J_c from that used in LTS materials, namely incorporating additional strong grain and grain boundary pinning sites in microcrystalline materials to produce high J_c values. $\text{Bi}_2\text{Sr}_2\text{Ca}_2\text{Cu}_3\text{O}_{10}$: both our micro- and nanocrystalline samples have ρ_{GB}/ρ_G of at least 10^3 . This causes strong suppression of J_c across the grain boundaries, which explains the low transport J_c values we find experimentally. Our calculations show that low J_c in untextured polycrystalline $\text{Bi}_2\text{Sr}_2\text{Ca}_2\text{Cu}_3\text{O}_{10}$ material is to be expected and the significant effort in the community in texturing samples and removing grain boundaries altogether is well-founded.

Keywords: superconductivity, critical current, $\text{Bi}_2\text{Sr}_2\text{CaCu}_2\text{O}_8$, $\text{Bi}_2\text{Sr}_2\text{Ca}_2\text{Cu}_3\text{O}_{10}$, nanocrystalline, weak-link

(Some figures may appear in colour only in the online journal)

1. Introduction



Original content from this work may be used under the terms of the [Creative Commons Attribution 3.0 licence](#). Any further distribution of this work must maintain attribution to the author(s) and the title of the work, journal citation and DOI.

High critical current density (J_c) in superconducting materials is usually the most important technological figure of merit. In high fields, this requires both a high current density associated with flux pinning (J_p) and a high depairing current density (J_{Dsc})

throughout the entire material. A high pinning current density (J_p) ensures that there are large forces, called pinning forces, that prevent the fluxons from moving. In polycrystalline low temperature superconductors (LTS), such large forces were often achieved by reducing the grain size. This increased the force necessary to drive fluxons along the grain boundaries, from one side of the sample to the other, by increasing the density of grain boundary triple points and the distortions of the fluxons required for them to move [2, 3]. In high temperature superconductors (HTS), the pinning force has often been increased by adding inclusions that pin each fluxon [4]. In properly optimised technological materials, in addition to high J_p , we must also ensure that J_{DSc} (the theoretical upper limit associated with the density of Cooper pairs in a material), is high enough to ensure J_c does not cause the pairs to break. In HTS, it is well established that large angle grain boundaries can cause J_c to drop by several orders of magnitude, depending on the misorientation angle [5–7]. This has become known as the ‘weak-link problem’, a problem so severe that the most important commercial HTS materials, $\text{YBa}_2\text{Cu}_3\text{O}_{7-x}$ (YBCO) and $\text{Bi}_2\text{Sr}_2\text{Ca}_2\text{Cu}_3\text{O}_{10}$, are produced in pseudo single-crystal tape and wire form. These forms require use of complex and expensive fabrication processes in order to minimise grain misalignment and eliminate high angle grain boundaries. Although historically, weak-links were uniquely identified by low J_c , it is important to identify why J_c is low – whether the grain boundary depairing current density (J_{DN}) is low or if there is low pinning (J_{PN}).

Although studying bicrystal systems has contributed to our understanding, because they provide a route to study grain boundaries with precisely fabricated boundaries and misorientation angles [5–7] and can be considered the building blocks for polycrystalline materials, most measurements do not include reports of local values of J_{DN} and J_{PN} . Furthermore, it is not straightforward to relate the behaviour of a bicrystal to the role of the equivalent grains or grain boundary in a polycrystalline material. For example, we have long known that notches or flaws [8] as well as the surface conditions or coatings [9] in single crystals strongly affect their current carrying capacity and that the topology of, and hence the pinning by, grain boundaries in polycrystalline materials is very important and quite different to that found in the broadly planar grain boundaries in bicrystal studies. For the bicrystal grain boundaries to have transport properties in the superconducting state that are closer to those found in polycrystalline samples, they would need to include the complicated topology of the grain boundaries in polycrystalline materials and have the surface pinning removed, that can be expected at the superconductor-air and superconductor-substrate interfaces in bicrystal systems.

Given the uncertainties in the potential for grain boundaries in HTS materials to carry high critical current densities in high fields and the importance of driving down the cost of HTS materials with high J_c for applications such as fusion [10, 11], we have decided to investigate micro- and nanocrystalline HTS materials further. This approach means we focus our efforts on the specific properties and challenges associated with the complex grain boundaries found in more practical, and potentially more technologically important, polycrystalline materials. We have already reported results on polycrystalline $\text{YBa}_2\text{Cu}_3\text{O}_7$ (YBCO)

with micro- and nano-sized grains that included measurements and calculations of angular averaged grain boundary resistivities [1]. Following work on S-N-S junctions that showed it was possible to relate the resistivity of junctions to the local depairing current density [12], we found that for most LTS, MgB_2 , iron-based superconductors and YBCO, even if the grain boundaries are non-superconducting, if their resistivity is equal to that of the grains, they have a J_{DN} that is only about a factor of five lower than the depairing current density. Equally we found the conditions in which resistive grain boundaries severely depress the local current density (i.e. to produce low J_{DN}).

In this paper, we look at the Bi-based materials that have the chemical formula $\text{Bi}_2\text{Sr}_2\text{Ca}_{n-1}\text{Cu}_n\text{O}_{2n+4}$ (BiSCCO) where $n = 1, 2, 3$ gives the first three members of this class: $\text{Bi}_2\text{Sr}_2\text{CuO}_6$, $\text{Bi}_2\text{Sr}_2\text{CaCu}_2\text{O}_8$ and $\text{Bi}_2\text{Sr}_2\text{Ca}_2\text{Cu}_3\text{O}_{10}$, with critical temperatures (T_c) of 20 K, 85 K and 110 K respectively. These materials have a layered structure and the anisotropy of the unit cell lattice parameters increases with n . We consider in detail $\text{Bi}_2\text{Sr}_2\text{CaCu}_2\text{O}_8$ and $\text{Bi}_2\text{Sr}_2\text{Ca}_2\text{Cu}_3\text{O}_{10}$. They are complex materials with flux lines that can behave as vortex pancakes [13] and have vortex states including vortex liquids, glasses and solids in their field-temperature phase diagram [14–16]. They have a much higher carrier mass anisotropy than YBCO, their flux-line lattices melt at fields and temperatures much lower than YBCO [17] and the irreversibility fields (B_{Irr}) in BiSCCO are significantly lower than YBCO at temperatures above 10 K [18]. Nevertheless, although an extrapolation of both upper critical field (B_{c2}) and B_{Irr} to 0 K for BiSCCO has a large uncertainty, the critical fields for $\text{Bi}_2\text{Sr}_2\text{CaCu}_2\text{O}_8$ and $\text{Bi}_2\text{Sr}_2\text{Ca}_2\text{Cu}_3\text{O}_{10}$ are estimated to be of the order of a few hundred Tesla, which is clearly sufficient for high-field applications [14, 18–20].

In addition to high critical fields, potentially useful high-field technological superconductors must also have high J_{DSc} . Table 1 shows the J_{DSc} for $\text{Bi}_2\text{Sr}_2\text{CaCu}_2\text{O}_8$ and $\text{Bi}_2\text{Sr}_2\text{Ca}_2\text{Cu}_3\text{O}_{10}$, and the parameters used to calculate them [1]. The angular averaged depairing current densities ($\langle J_{DSc}(0, T) \rangle$) were calculated using

$$\langle J_{DSc}(0, T) \rangle = \frac{\Phi_0}{3\sqrt{3}\pi\mu_0} \left\langle \frac{1}{\lambda^2(T)\xi(T)} \right\rangle, \quad (1)$$

where $\left\langle \frac{1}{\lambda^2(T)\xi(T)} \right\rangle$ can be calculated from the anisotropic λ and ξ values in table 1. We have chosen to calculate the values of λ_{ab} and ξ_{ab} from B_{c2}^c and B_{cl}^c . The values of λ_c and ξ_c were then derived from the mass anisotropy ratio γ , where we have used $\gamma = \frac{dB_{c2}^b}{dT} / \frac{dB_{c2}^c}{dT} \approx 10$ [21] and 7 [22]. Higher values of γ have also been reported [17], but these do not significantly change our calculated values for angular averages of any of the critical parameters. The large ratio of J_{DSc} along the ab -plane to the c -axis direction led to the railway switch model which described current flowing preferentially along the ab -planes [23]. Useful J_c values have already been achieved in both $\text{Bi}_2\text{Sr}_2\text{CaCu}_2\text{O}_8$ and $\text{Bi}_2\text{Sr}_2\text{Ca}_2\text{Cu}_3\text{O}_{10}$ conductors. $\text{Bi}_2\text{Sr}_2\text{CaCu}_2\text{O}_8$ can produce high J_c in round wire form, due to its quasi-biaxial textured grain structure [19, 24, 25]. $\text{Bi}_2\text{Sr}_2\text{Ca}_2\text{Cu}_3\text{O}_{10}$ tapes have a uniaxial c -axis texture with high J_c in tapes and wires [26–28]. It is clear that removing grain boundaries or producing materials that only incorporate low-angle grain boundaries can produce high J_c . Nevertheless, at 0 T and 4.2 K, J_c/J_{DSc} is still approximately

Table 1. The depairing current density at zero magnetic field and 4.2 K, $J_{\text{DSc}}(0 \text{ T}, 4.2 \text{ K})$, and the parameters used to calculate it. T_c is the critical temperature, ν is the exponent derived from fitting the empirical equation for the temperature dependence of the upper critical field in $B_{\text{c}2}^{\text{c}}(T) = B_{\text{c}2}^{\text{c}}(0)(1 - (T/T_c)^{\nu})$ to single-crystal data along the c -axis. We have assumed a similar temperature dependence for fields applied along the ab -plane. We have used a mass anisotropy ratio $\gamma = \frac{dB_{\text{c}2}^{\text{ab}}}{dT}/\frac{dB_{\text{c}2}^{\text{c}}}{dT} \approx 10$ [21] and 7 [22] for $\text{Bi}_2\text{Sr}_2\text{CaCu}_2\text{O}_8$ and $\text{Bi}_2\text{Sr}_2\text{Ca}_2\text{Cu}_3\text{O}_{10}$ respectively. The G–L coherence length and G–L penetration depth are given parallel to the ab -plane and parallel to the c -axis at 0 K and have been calculated using the temperature dependence of the critical fields close to T_c [1]. We note that a very rough estimate of the coherence length at low temperature can also be calculated (not shown here) using the Ginzburg–Landau equation $\xi_{B_{\text{c}2}}(T) = (\Phi_0/2\pi B_{\text{c}2}(T))^{\frac{1}{2}}$, although strictly the equation is only valid close to T_c . Parameters that were obtained from temperature dependent experiments in the literature have the relevant reference cited next to them. Calculated parameters are labelled with *. For $\text{Bi}_2\text{Sr}_2\text{Ca}_2\text{Cu}_3\text{O}_{10}$: we chose the value for ν to be the same as for $\text{Bi}_2\text{Sr}_2\text{CaCu}_2\text{O}_8$ (i.e. 0.14).

Material	T_c (K)	ν	$B_{\text{c}2}(0)$ (T)	$B_{\text{c}1}(0)$ (mT)	$\xi(0)$ (nm)	$\lambda(0)$ (nm)	$J_{\text{DSc}}(0, 4.2)$ (A m^{-2})
$\text{Bi}_2\text{Sr}_2\text{CaCu}_2\text{O}_8$	84.8 [84]	$ab:$	2310*	1.34*	3.24*	300 [84]	$3.21 \times 10^{11*}$
		$c:$	0.14 [20]	231 [20]	4.60*	0.324*	$3.21 \times 10^{10*}$
		$\langle \rangle:$			2.28*	500*	$2.21 \times 10^{11*}$
$\text{Bi}_2\text{Sr}_2\text{Ca}_2\text{Cu}_3\text{O}_{10}$	108 [85]	$ab:$	2080*	5.61*	2.86*	165 [86]	$1.22 \times 10^{12*}$
		$c:$	0.14	297 [85]	13.8*	0.408*	$1.74 \times 10^{11*}$
		$\langle \rangle:$			2.04*	262*	$8.56 \times 10^{11*}$

Table 2. The nanocrystalline samples in this paper and their fabrication process. ‘B1’ and ‘B2’ represent Bi-2212 and Bi-2223 respectively. Letters ‘P’, ‘M’, ‘H’, and ‘A’ stand for pressed, milled, HIP’ed and annealed respectively. The numbers following ‘M’ shows the milling time in minutes. HIP processing was at 450 °C and 177 MPa for 5 h. Letter ‘A’ followed by a number denotes the maximum annealing temperature used, the details can be found in this table. The grain size of B2M30HA750 was 200 nm and has been taken as representative of all nanocrystalline materials and denoted using the symbol ‘†’.

Sample	Grain size (nm)	Annealing process
B1P	5000	—
B1HA750	5000	750 °C for 20 h then 450 °C for 60 h
B1M30P	3.6	—
B1M60P	2.8	—
B1M30H	70	—
B1M30HA500	200†	500 °C for 5 h then 450 °C for 20 h
B1M30HA750	200†	750 °C for 20 h then 450 °C for 60 h
B1M60HA750	200†	750 °C for 20 h then 450 °C for 60 h
B1M60HA800	200†	800 °C for 20 h then 450 °C for 60 h
B2P	5000	—
B2HA750	5000	750 °C for 20 h then 450 °C for 60 h
B2M30P	9.8	—
B2M60P	3.6	—
B2M30H	70	—
B2M30HA500	200†	500 °C for 5 h then 450 °C for 20 h
B2M30HA750	200	750 °C for 20 h then 450 °C for 60 h
B2M60HA750	200†	750 °C for 20 h then 450 °C for 60 h
B2M60HA800	200†	800 °C for 20 h then 450 °C for 60 h

only 10^{-2} and 10^{-3} for Bi-2212 and Bi-2223 respectively, showing that further large increases in J_c are still possible in these materials. However, in this paper, our approach is quite different to that of eliminating high angle grain boundaries. We fabricate and measure bulk micro- and nanocrystalline $\text{Bi}_2\text{Sr}_2\text{CaCu}_2\text{O}_8$ and $\text{Bi}_2\text{Sr}_2\text{Ca}_2\text{Cu}_3\text{O}_{10}$ materials using well-established powder metallurgy techniques because of their significant potential for use in a conductor technology. Using our measurements and analysis, we try to identify the potential these polycrystalline materials have – more specifically what mechanism limits J_c and are there any approaches for producing relatively cheap high J_c randomly-aligned polycrystalline BiSCCO materials that will lead to conductors that make new high-field superconducting applications cost-effective?

The paper is structured as follows: the fabrication process and microstructure characterisation is presented in section 2. The transport and magnetisation measurement results are shown in section 3. Section 4 presents some theoretical considerations and section 5 discusses the important results. Finally, our conclusions are summarised in section 6.

2. Fabrication of polycrystalline materials

2.1. Sample fabrication

Commercial $\text{Bi}_2\text{Sr}_2\text{CaCu}_2\text{O}_8$ (B1) and $\text{Bi}_2\text{Sr}_2\text{Ca}_2\text{Cu}_3\text{O}_{10}$ (B2) powders (99.98%, purchased from Toshima [29]) were used to fabricate the micro- and nanocrystalline samples. The powders were milled using a SPEX 8000D high-energy shaker mill, with

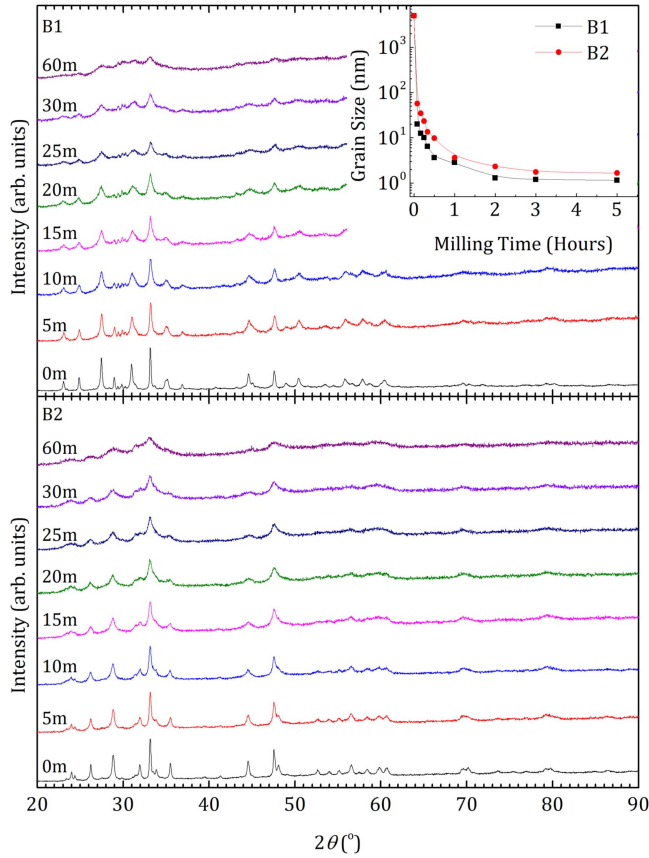


Figure 1. XRD patterns of B1 (upper panel) and B2 (lower panel) samples. From the bottom to the top, the traces in each panel are: as-supplied material, milled 5, 10, 15, 20, 25, 30 and 60 min samples. Inset: grain size as a function of milling time for both B1 and B2.

tungsten carbide (WC 94/Co 6) milling media in an argon atmosphere. The samples were milled in batches of 10 g with a ball-to-powder mass ratio of 3:1 for either 30 or 60 min. The milling vial and balls were regularly scraped with a tungsten carbide rod in an argon atmosphere within a glovebox, to increase yield and improve homogeneity. After milling, magnetic separation [30] was employed to remove Co contamination in the milling media from the milled powdered samples using a 0.7 T iron-core magnet. The powders were placed into niobium foil packets (0.025 mm thick, 99.8%, Alfa Aesar), that acted as diffusion barriers, sealed into stainless steel tubes (type 316, 1 mm thickness) and then consolidated using a hot isostatic press (HIP) at a temperature of 450 °C and pressure of 177 MPa for 5 h. The pressure, 177 MPa, was the practical limit for the HIP. Samples were subsequently annealed in a pure flowing oxygen atmosphere in a dedicated oxygen furnace to optimise oxygen content and restore some crystallinity. We chose to anneal our samples at 750 °C, following Zhao *et al* [31], and also at 500 °C and 800 °C. In this paper, the letters ‘P’, ‘M’, ‘H’ and ‘A’ denote that a sample has been processed through a combination of pellet pressing, milling, HIP’ing and annealing respectively. The magnetic separation process was used on all our milled samples. The numbers 30 and 60 following ‘M’ indicate the milling time in minutes. The numbers following the letter ‘A’ denote the annealing temperature in degrees Celsius. Table 2 lists the details

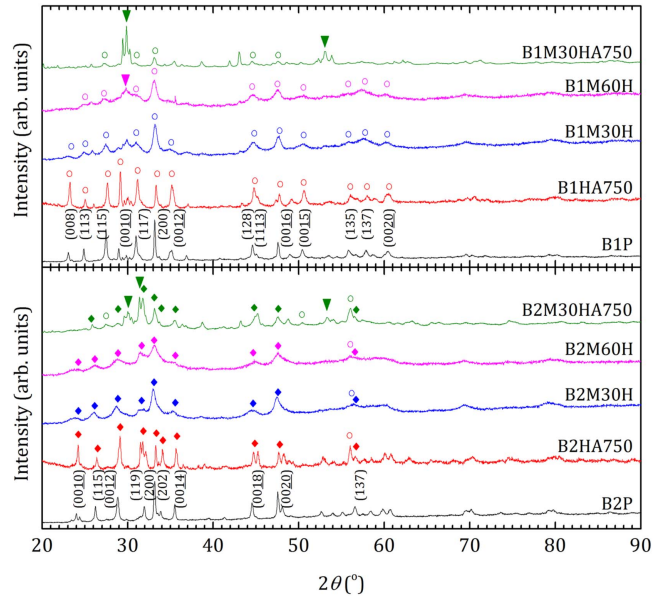


Figure 2. XRD of B1 (upper panel) and B2 (lower panel) samples. From the bottom to top, the traces in each panel are: as-supplied material, HA750, M30H, M60H and M30HA750 samples. The main $\text{Bi}_2\text{Sr}_2\text{CuO}_6$, $\text{Bi}_2\text{Sr}_2\text{CaCu}_2\text{O}_8$ and $\text{Bi}_2\text{Sr}_2\text{Ca}_2\text{Cu}_3\text{O}_{10}$ peaks are labelled with ‘▼’, ‘○’ and ‘◆’ symbols respectively.

of the fabrication process for all microcrystalline and nanocrystalline samples in this paper. A full set of measurements was completed on four samples, which includes a micro- and a nanocrystalline sample for both B1 and B2, namely: B1HA750, B1M30HA750, B2HA750 and B2M30HA750.

2.2. X-ray diffraction (XRD)

The grain sizes of the samples were obtained using powder XRD measurements. Figure 1 shows the evolution of the XRD spectra for the as-supplied material, and after they were milled for 5, 10, 15, 20, 25, 30 and 60 min. The XRD peaks broadened with increased milling time in a similar way for both B1 and B2. The grain size was obtained by Rietveld refinement using TOPAS Academic software. The inset shows the grain size as a function of milling time. After 30 min of milling, the grain size reduced to <10 nm. No decrease in grain size was observed for milling times greater than 3 h.

Figure 2 shows the powder XRD spectra for both B1 and B2 of the as-supplied, M30H, M60H and M30HA750 samples. HA750 data are also shown for a solid flat piece of sample. The main $\text{Bi}_2\text{Sr}_2\text{CuO}_6$, $\text{Bi}_2\text{Sr}_2\text{CaCu}_2\text{O}_8$ and $\text{Bi}_2\text{Sr}_2\text{Ca}_2\text{Cu}_3\text{O}_{10}$ peaks are labelled with ‘▼’, ‘○’ and ‘◆’ symbols respectively. For both sets of samples, the peak positions of the HA750, M30H and M60H samples are still largely the same as the as-supplied material. The changes in the relative peak intensities show that the samples are textured. The peaks of the milled samples were broad but some crystallinity was restored after annealing. The microcrystalline HA750 materials are predominantly single phase. The M30H and M60H materials are also predominantly single phase, but have low superconducting critical parameters. The annealed samples have superconductivity restored but are mixed $\text{Bi}_2\text{Sr}_2\text{Ca}_{n-1}\text{Cu}_n\text{O}_{2n+4}$ phases with some additional

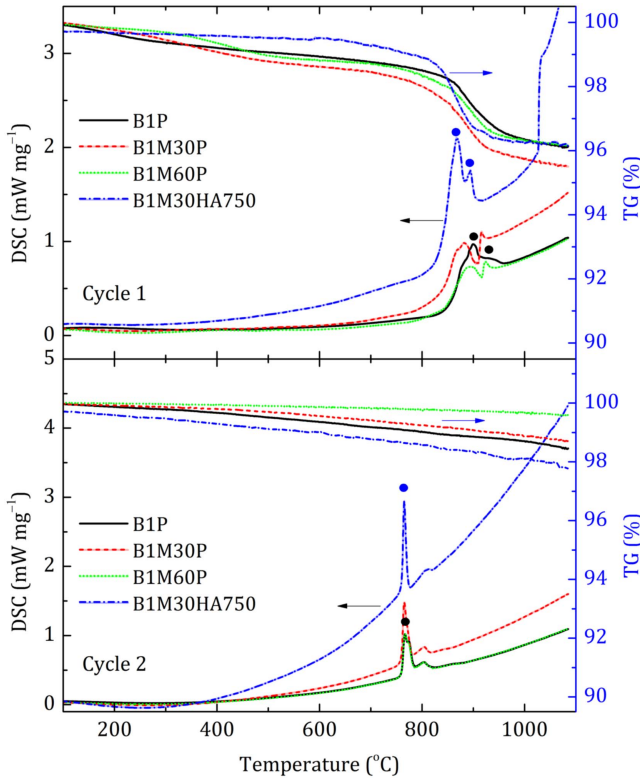


Figure 3. Differential scanning calorimetric (DSC) signal and thermogravimetric (TG) signal of B1P, B1M30P, B1M60P and B1M30HA750 samples between 100 °C and 1100 °C, ramped at 10 °C min⁻¹. Top: first run, bottom: second run. Significant endothermic peaks, associated with melting are labelled with ● symbols. No crystallisation peaks are seen in the milled materials.

secondary phase material. The grain sizes of all samples are listed in table 2. Accurate values for the nanocrystalline sample B2M30HA750 were obtained and taken to be representative of all nanocrystalline samples because of the large uncertainties found for the other nanocrystalline materials.

2.3. Thermo gravimetry (TG)/differential scanning calorimetry (DSC)

Figure 3 shows DSC and TG data for the P, M30P, M60P and M30HA750 samples for B1. The same data for B2 are shown in figure 4. Data were obtained over two cycles. In each cycle, samples were heated up to 1100 °C and cooled back to room temperature in a pure argon atmosphere at 10 °C min⁻¹. We identify the main endothermic DSC peaks as follows: the peak near 890 °C in the B1P sample corresponds to the melting of the Bi₂Sr₂CaCu₂O₈ phase and the peaks near ~940 °C in B1P corresponds to melting of the (Sr,Ca)CuO₂ and (Sr,Ca)₂CuO₃ phases that grow from the Bi₂Sr₂CaCu₂O₈ melt [32, 33]. After milling, these melting temperatures were lowered. In the case of B1M30HA750, the melting of the Bi₂Sr₂CaCu₂O₈ was lowered to ~870 °C and the (Sr,Ca)_xCuO_y phases was lowered to ~890 °C. In the second cycle of B1 samples, the peak near 780 °C in cycle 2 of the B1 and B2 materials may be melting of Bi₂O₃ or the polymorphous transition of Bi₂O₃ $\alpha \rightarrow \beta$ [33]. The peak near 875 °C in the B2P sample corresponds to melting of the Bi₂Sr₂Ca₂Cu₃O₁₀ phase [33–35], and the peak near 920

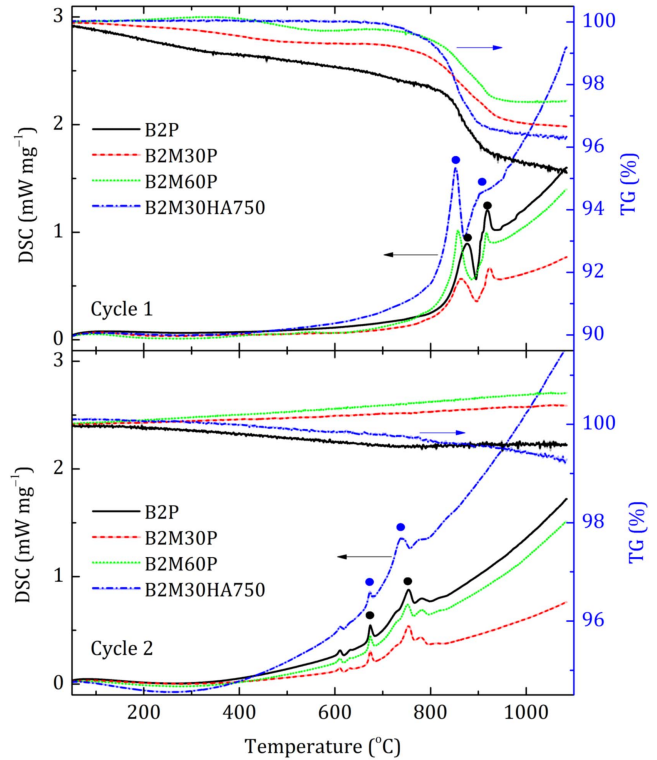


Figure 4. Differential scanning calorimetric (DSC) signal and thermogravimetric (TG) signal of B2P, B2M30P, B2M60P and B2M30HA750 samples between 100 °C and 1100 °C, ramped at 10 °C min⁻¹. Top: first run, bottom: second run. Significant endothermic peaks, associated with melting are labelled with ● symbols. No crystallisation peaks are seen in the milled materials.

corresponds to melting of the Bi₂Sr₂CuO₆, (Sr,Ca)CuO₂ and Ca₂CuO₃ phases [36]. After milling, the melting temperature of the Bi₂Sr₂Ca₂Cu₃O₁₀ phase was lowered to 850 °C. The peaks at 650 °C–680 °C in cycle 2 of the B2 materials may be Bi₂Sr₂CuO₆ + Ca₂CuO₃ + CuO \rightarrow Bi₂Sr₂CaCu₂O₈ + Ca₂CuO₅ + CuO [36]. Generally, in nanocrystalline or amorphous materials, small exothermic peaks are observed in the milled materials, which identifies the temperature at which crystallisation occurs [1, 37–39]. B1 and B2 are very soft, thus the energy associated with crystallisation is expected to be small. Unfortunately, no exothermic crystallisation peaks are seen in figure 3 for the milled B1 and B2 materials. We confirm that annealing temperatures above 450 °C in oxygen were required to recover superconductivity in milled samples [31], and so we chose this low temperature for HIP'ing to minimise crystal growth.

3. Experimental results and analysis

3.1. Resistivity measurements

For transport measurements, samples were shaped into cuboid bars using fine Emery paper with typical dimensions of 1 × 1 × 8 mm. The samples were mounted onto a physical property measurement system (PPMS) resistivity puck [40]. Current and voltage leads were connected to the samples

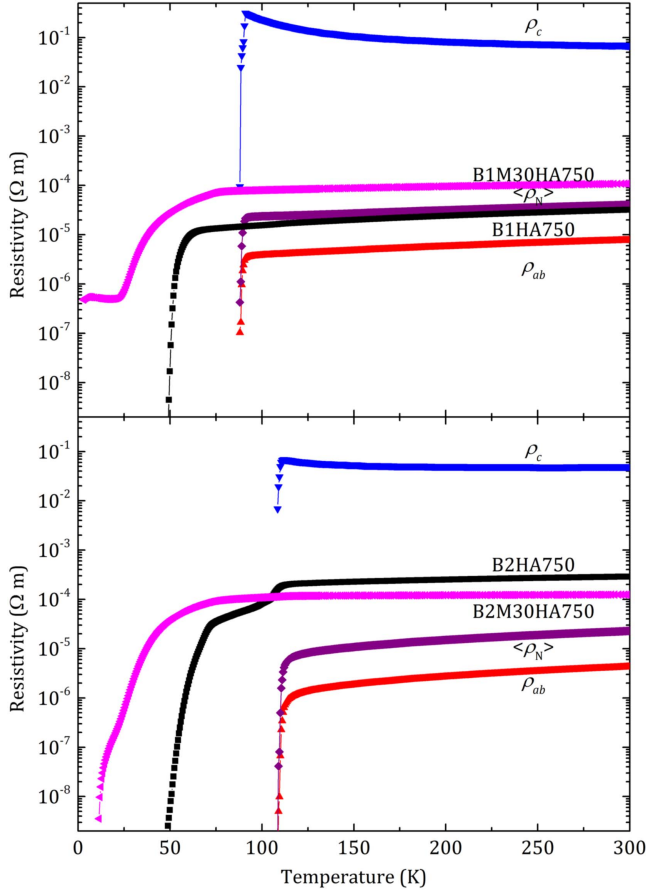


Figure 5. Resistivity as a function of temperature for $\text{Bi}_2\text{Sr}_2\text{Ca}\text{Cu}_2\text{O}_8$ (upper panel) and $\text{Bi}_2\text{Sr}_2\text{Ca}_2\text{Cu}_3\text{O}_{10}$ (lower panel) micro-(HA750) and nanocrystalline (M30HA750) materials in zero field.

using silver paint for standard four-terminal measurements. The voltage taps were typically 5 mm apart. The temperature and the magnetic field were controlled and measured using the PPMS.

Figure 5 shows the resistivity as a function of temperature for the four most important samples, B1HA750, B1M30HA750, B2HA750 and B2M30HA750, measured using excitation currents of typically 5 mA. Single crystal resistivity of $\text{Bi}_2\text{Sr}_2\text{Ca}\text{Cu}_2\text{O}_8$ [41] and $\text{Bi}_2\text{Sr}_2\text{Ca}_2\text{Cu}_3\text{O}_{10}$ [42] along the ab -plane (ρ_{ab}) and c -axis (ρ_c) are also shown on each graph. The angular averaged resistivity ($\langle \rho_N \rangle$), calculated from the single-crystal data and discussed below, are also shown. Figures 6 and 7 show the in-field resistivity for each of the four samples and the irreversibility field derived using criteria of 90%, 50%, 10% and 0% of $\rho_N(T_c)$. Both the B1HA750 sample and the B1M30HA750 sample in figure 6 shows similar superconducting transitions at 75 K due to the $\text{Bi}_2\text{Sr}_2\text{Ca}\text{Cu}_2\text{O}_8$ phase where the onset (see 90% of $\rho_N(T_c)$) is only weakly sensitive to magnetic field. However, the two materials reach zero resistivity at quite different fields and temperatures (see 0% of $\rho_N(T_c)$). We associate these differences with the much poorer properties of the grain boundaries in the nanocrystalline material. Similar behaviour has been reported elsewhere in $\text{Bi}_2\text{Sr}_2\text{Ca}\text{Cu}_2\text{O}_8$ bicrystals and polycrystalline material [43, 44]. Figure 7 shows equivalent data

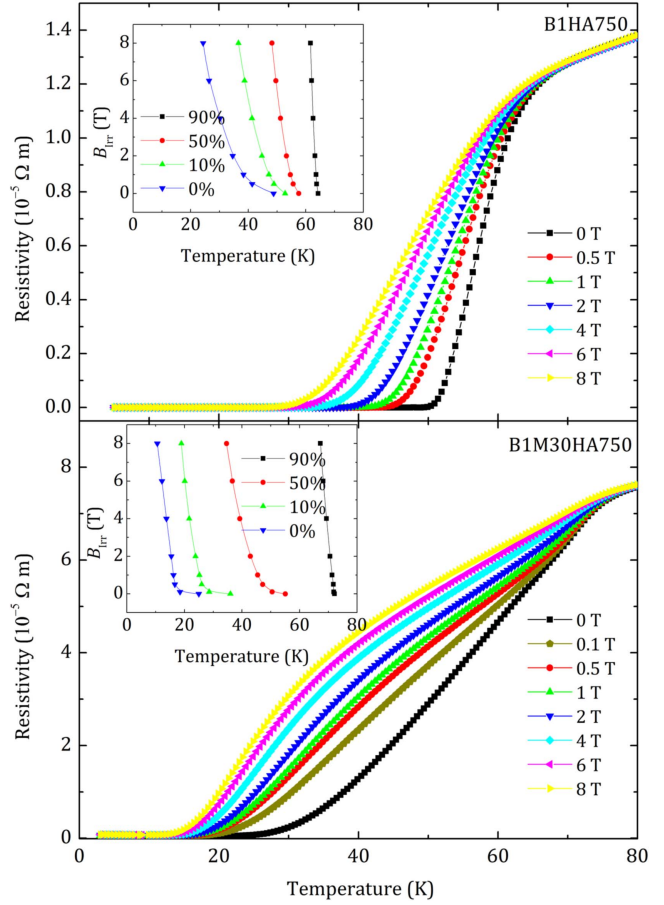


Figure 6. Upper panel: resistivity of the B1HA750 sample measured in fields of 0–8 T with a constant excitation current of 5 mA. Inset: B_{irr} determined using the criteria of 90%, 50% and 10% of $\rho_N(0 \text{ T}, 70 \text{ K})$, and onset of zero resistivity (0% ρ_N). Lower panel: equivalent data for the B1M30HA750 sample.

for the B2HA750 and B2M30HA750 samples. Both materials show a transition at 110 K due to the optimally doped $\text{Bi}_2\text{Sr}_2\text{Ca}_2\text{Cu}_3\text{O}_{10}$ phase which is also only weakly sensitive to field. A second superconducting transition at 75 K occurs in both materials due to $\text{Bi}_2\text{Sr}_2\text{Ca}\text{Cu}_2\text{O}_8$. In the B2M30HA750 sample, the reduction in resistivity between 110 and 75 K is small in comparison to B2HA750, indicative of a much larger content of $\text{Bi}_2\text{Sr}_2\text{Ca}\text{Cu}_2\text{O}_8$ in the milled material.

3.2. Ac magnetic susceptibility

Ac magnetic susceptibility measurements were taken using a Quantum Design PPMS system [45] as a function of field (up to 8 T) and temperature, with an excitation field of 0.4 mT operating at 777 Hz. The non-HIP'ed samples were pressed into pellets. HIP'ed samples were shaped into cuboids or bars using fine grit Emery paper. A collation of all zero-field ac magnetic susceptibility for B1 samples is shown in figure 8, where the onset transitions are shown in the main figure and the complete data sets are shown in the inset. We have also calculated T_c values by extrapolating the large signal data for which the

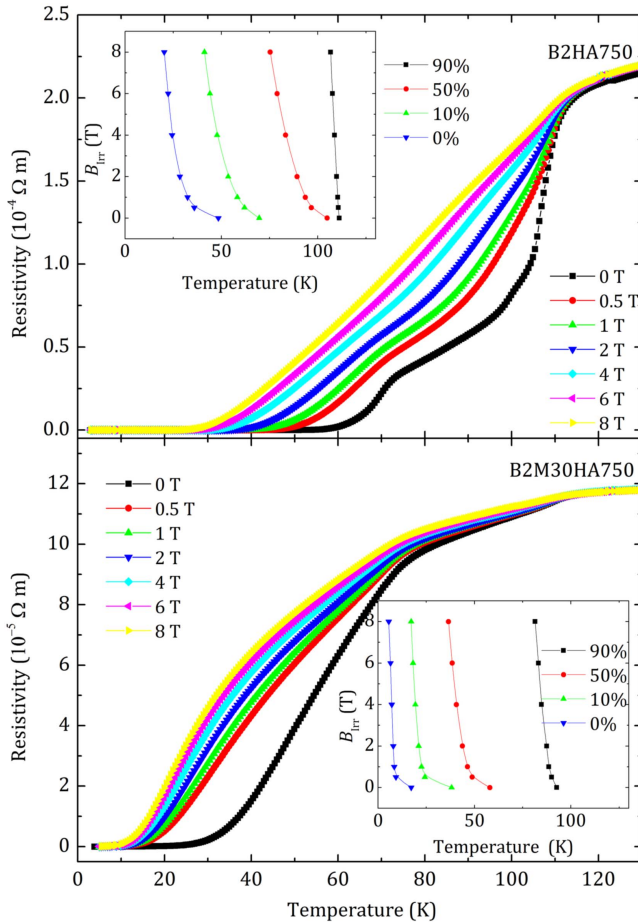


Figure 7. Upper panel: resistivity of the B2HA750 sample measured in fields of 0–8 T with a constant excitation current of 5 mA. Inset: B_{Irr} determined using the criteria of 90%, 50% and 10% of ρ_N (0 T, 120 K), and zero resistivity (0% ρ_N). Lower panel: Equivalent data for the B2M30HA750 sample.

magnitude of the susceptibility is typically a few percent of full screening and listed them in table 3. The pressed sample and the B1HA750 sample were not of standard shape so we have normalised their susceptibility to be -1 at the lowest temperatures. The as-supplied material B1P and unmilled material B1HA750 contains significant $\text{Bi}_2\text{Sr}_2\text{Ca}_2\text{Sr}_3\text{O}_{10}$, as evidenced by their onset values close to 105 K. However, a large signal associated with the $\text{Bi}_2\text{Sr}_2\text{CaSr}_2\text{O}_8$ phase and bulk screening, leading to transmission of current across grain boundaries occurs below 75.2 K and 72.1 K respectively. The milling process almost completely removed all superconductivity. The milled, unannealed samples, B1M30P, B1M60P, B1M30H and the sample annealed at the lowest temperature, B1M30HA500, all showed similar behaviour – a weak or no diamagnetic signal generally followed by a paramagnetic temperature dependence, similar to that seen in YBCO after milling [1, 46, 47]. All the annealed samples show that superconductivity has been recovered with onset signals near 75 K, associated with the grains. At lower temperatures, large signals occur as the grain boundaries support significant screening currents. Figure 9 shows the in-field susceptibility of the B1HA750 sample, and

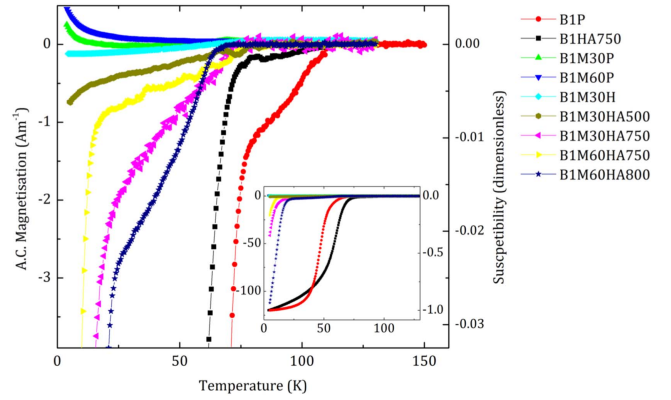


Figure 8. Ac magnetisation and magnetic susceptibility of all B1 samples in zero field. The data were taken with an excitation field of 0.4 mT at a frequency of 777 Hz. Inset: equivalent large signal data.

the equivalent data for the B1M30HA750 sample are shown in the inset. The B1HA750 sample shows an onset T_c at 70 K in zero field. At lower temperatures, the sample shows full-screening and most notably (as discussed in section 3.3), values of $\mu_0 \Delta M / \Delta B$ close to Bean values of -0.17 , similar to a low temperature polycrystalline superconductor with well-connected grains or a single-crystal superconductor. In contrast, the B1M30HA750 sample shows granular behaviour [1, 48, 49] and does not reach full screening. We have measured all the B1 samples in-field and used the onset and large signal data to produce irreversibility fields associated with each signal and provided them in figure 10. The upper and lower panels show the onset and large signal B_{Irr} values respectively. In order to obtain estimates of $B_{\text{Irr}}(0)$, the temperature dependence of the data were generally characterised using the equation [50]:

$$B_{\text{Irr}}(T) = B_{\text{Irr}}(0)(1 - t^{0.5})^{2.1}, \quad (2)$$

where $t = T/T_c$. Although for some large signal, nanocrystalline materials, a linear fit was used. Figure 10 shows that the irreversibility fields are high and similar to the upper critical field values along the c -axis for $\text{Bi}_2\text{Sr}_2\text{CaCu}_2\text{O}_8$ [18, 20]. Similar compilations for all the B2 samples are also provided. Figure 11 shows all zero-field ac magnetic susceptibility and figure 12 shows the irreversibility fields. All onset and large signal values of T_c , and $B_{\text{Irr}}(0)$, can be found in table 3. The milled, unannealed materials were again either only weakly diamagnetic or paramagnetic. Annealing was required to recover superconductivity in these materials. Irreversibility fields were again high at low temperature for some of these B2 materials [18]. Even though full screening is recovered in some samples, it is important to note that the full screening of a 0.4 mT signal is not indicative of well-connected grains with grain boundaries carrying high current densities.

The susceptibility data can be used to estimate whether the supercurrent screening path is inter- or intragranular. If the screening currents are entirely intragranular, the susceptibility is reduced by a factor χ'_g/χ'_b where [48, 49]:

$$\frac{\chi'_g}{\chi'_b} = \frac{1}{15} \left(\frac{a^2}{\lambda^2} \right) f(a, \xi_{\text{BCS}}) \text{ for } \lambda > a, \quad (3)$$

Table 3. Summary of critical temperature (T_c), irreversibility field ($B_{\text{Ir}}(0)$), magnetisation and transport critical current density (J_c^m and J_c^t) and room temperature normal state resistivity (ρ_N) of fabricated samples. ‘B1’ and ‘B2’ represent Bi-2212 and Bi-2223 respectively. Letters ‘P’, ‘M’, ‘H’, and ‘A’ stands for pressed powders, milled, HIP’ed and annealed respectively. T_c was determined from the onset (typical $\sim 10^{-4}$ of full screening) or large signal (typical $\sim 10^{-2}$ of full screening) of ACMS data. The symbol * suggests that a minority phase denoted the onset. ‘Para’ indicates a sample that behaved paramagnetically with no T_c found. $B_{\text{Ir}}(0)$ was calculated using in-field susceptibility data and extrapolating to zero temperature using equation (2). χ'_g/χ'_b is the ac magnetic susceptibility data at 0 T and 4.2 K. $\mu_0 \Delta M/\Delta B$ is from dc magnetisation hysteresis measurements. J_c^m is at 4.2 K, calculated using sample dimensions for B1HA750 and the grain size for all other samples. J_c^t used a 1 mV m⁻¹ criterion.

Sample	T_c (K) Onset/ large signal	$B_{\text{Ir}}(0)$ (T) Onset/ large signal	$\frac{\chi'_g}{\chi'_b}$ (0 T, 4.2 K)	$\frac{\mu_0 \Delta M}{\Delta B}$ (-1.5 T)	J_c^m (0 T, 4.2 K) (A m ⁻²)	J_c^t (A m ⁻²)	ρ_N (300 K) (Ωm^{-1})
B1P	105*	63.1	1	-0.1	1.6×10^{10}	—	—
	67.6	49.2					
B1HA750	105*	84.8	1	-0.2	1.5×10^8	7.8×10^4 (4 T, 30 K)	3.2×10^{-5}
	54.0	78.6					
B1M30P	62.5	—	—	—	7.6×10^8	—	—
	Para	—					
B1M60P	Para	—	—	—	1.8×10^8	—	—
B1M30H	70.1	—	1.6×10^{-3}	—	7.6×10^9	—	—
	—	—					
B1M30HA500	76.4	75.4	6.2×10^{-3}	-6×10^{-4}	1.2×10^{10}	—	—
	—	—					
B1M30HA750	73.4	90.7	0.34	-3×10^{-3}	2.8×10^{10}	7.2×10^4 (0 T, 4.2 K)	1.1×10^{-4}
	10.5	34.3					
B1M60HA750	78.1	52.7	0.17	-2×10^{-3}	1.4×10^{10}	—	—
	8.4	48.2					
B1M60HA800	64.5	61.3	0.93	-5×10^{-3}	2.5×10^{10}	—	—
	16.7	34.4					
B2P	109.7	105.5	1	-0.4	5.1×10^{10}	—	—
	105.7	94.5					
B2HA750	107.3	57.4	0.97	-0.1	4.0×10^{10}	1.4×10^4 (1 T, 30 K)	2.9×10^{-4}
	107.1	51.0					
B2M30P	106.9	—	—	—	2.7×10^9	—	—
	Para	—					
B2M60P	Para	—	—	—	4.8×10^8	—	—
B2M30H	96.8	—	1.8×10^{-3}	—	1.0×10^{10}	—	—
	—	—					
B2M30HA500	90.6	81.8	6.0×10^{-3}	-9×10^{-4}	1.9×10^{10}	—	—
	—	—					
B2M30HA750	85.2	49.8	0.30	-3×10^{-3}	4.0×10^{10}	9.1×10^3 (0 T, 4.2 K)	1.2×10^{-4}
	13.5	1.56					
B2M60HA750	84.8	52.4	1.8×10^{-3}	-2×10^{-4}	4.8×10^9	—	—
	—	—					
B2M60HA800	61.9	53.5	0.95	-4×10^{-2}	2.3×10^{11}	—	—
	58.9	74.2					

and χ'_g and χ'_b are the granular and bulk (non-granular) susceptibilities respectively and a is the grain size. If we use the values $a = 200$ nm from table 2, and $\langle 1/\lambda^2 \rangle$ calculated using the data in table 1, we find $\chi'_g/\chi'_b = 1.5 \times 10^{-2}$ and 5.0×10^{-2} for B1 and B2 respectively. The values of χ'_g/χ'_b for all samples can be found in table 3. The calculated values are similar to the measured χ'_g/χ'_b for the samples where the grains are not well connected. For those samples where

$\chi'_g/\chi'_b \approx -1$, we find

$$\frac{\chi'_g}{\chi'_b} = 1 - \frac{3\lambda}{a} \text{ for } \lambda < a. \quad (4)$$

This gives a path size of $a \approx 2$ and $1 \mu\text{m}$ for B1M30HA750 and B2M30HA750, suggesting that these very small screening currents are not strictly confined within grains of 200 nm, and may flow around clusters of grains.

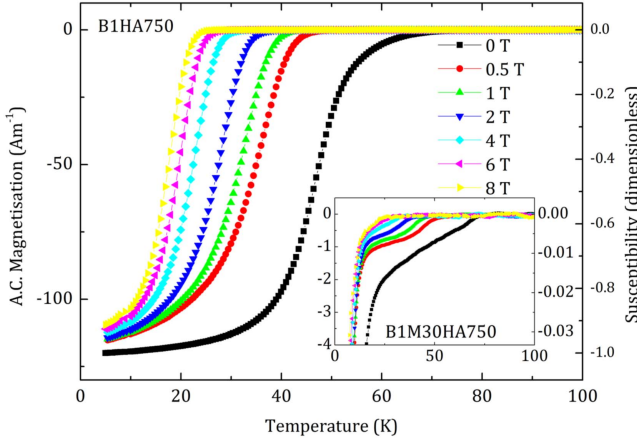


Figure 9. Ac magnetic susceptibility as a function of temperature of the B1HA750 sample. The data were taken with an excitation field of 0.4 mT and at a frequency of 777 Hz. Inset: equivalent data for the B1M30HA750 sample.

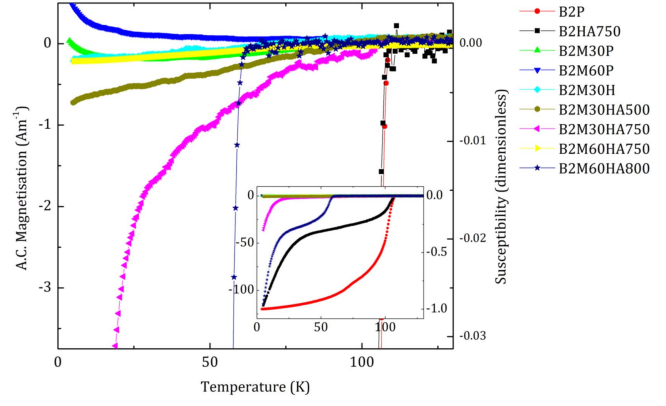


Figure 11. Ac magnetisation and magnetic susceptibility for all B2 samples in zero field. The data were taken with an excitation field of 0.4 mT at a frequency of 777 Hz. Inset: equivalent large signal data.

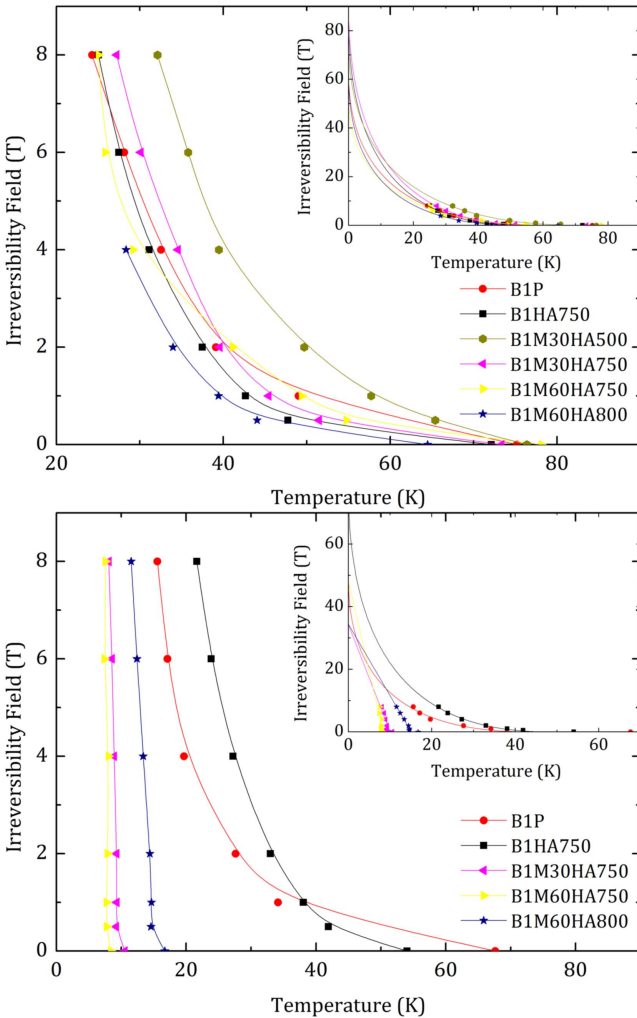


Figure 10. Irreversibility field as a function of temperature of all B1 samples. Upper panel: onset B_{irr} . Lower panel: large signal B_{irr} – obtained by extrapolating the large signal data for which the magnitude of the susceptibility is typically a few percent to zero signal. The data were fitted using equation (2) or linear fits to obtain values for $B_{\text{irr}}(0)$ as listed in table 3. Insets show the fitted curves over the full temperature range.

3.3. Dc magnetic hysteresis

Dc magnetisation hysteresis data were also taken with the PPMS. At each temperature, the field was swept from 0 T down to -1.5 T, then up to 8 T and back to -1.5 T. J_c values were calculated from these hysteresis data between 0 T and 8 T using Bean's model [51]. For pellets of radius R and volume V [52],

$$J_c = 3 \frac{\Delta m}{RV}, \quad (5)$$

where Δm is the difference in magnetic moment between the increasing and decreasing field branches. For rectangular bars with length w and width b [52],

$$J_c = \frac{2\Delta m}{w \left(1 - \frac{w}{3b}\right)V}. \quad (6)$$

Figures 13 and 14 show the hysteresis loops for B1HA750 and B1M30HA750 respectively. The microcrystalline B1HA750 sample shows typical Type-II behaviour for a polycrystalline sample with bulk pinning and well-connected grains. In contrast, the nanocrystalline B1M30HA750 sample shows a strong asymmetry about the baseline, with a large diamagnetic signal on increasing field and almost no signal on decreasing field. This behaviour has been reported in the literature and is associated with surface currents [53]. These asymmetric hysteresis loops were observed in all milled, HIP'ed and annealed materials. Figure 15 shows a compilation of the magnetisation J_c at 4.2 K for all the B1 samples and compares them with state-of-the-art Bi-2212 OP wires. The values shown for almost all the samples are intragranular values calculated using the grain size. The high intragranular values are comparable to and in many cases higher than state-of-the-art transport J_c in Bi-2212 OP wires. The only exception is the B1HA750 sample, where as we find in the next section, the magnetic signal is almost entirely due to intergranular currents flowing on the length scale of the sample, so we have used the sample dimensions to calculate J_c as shown in

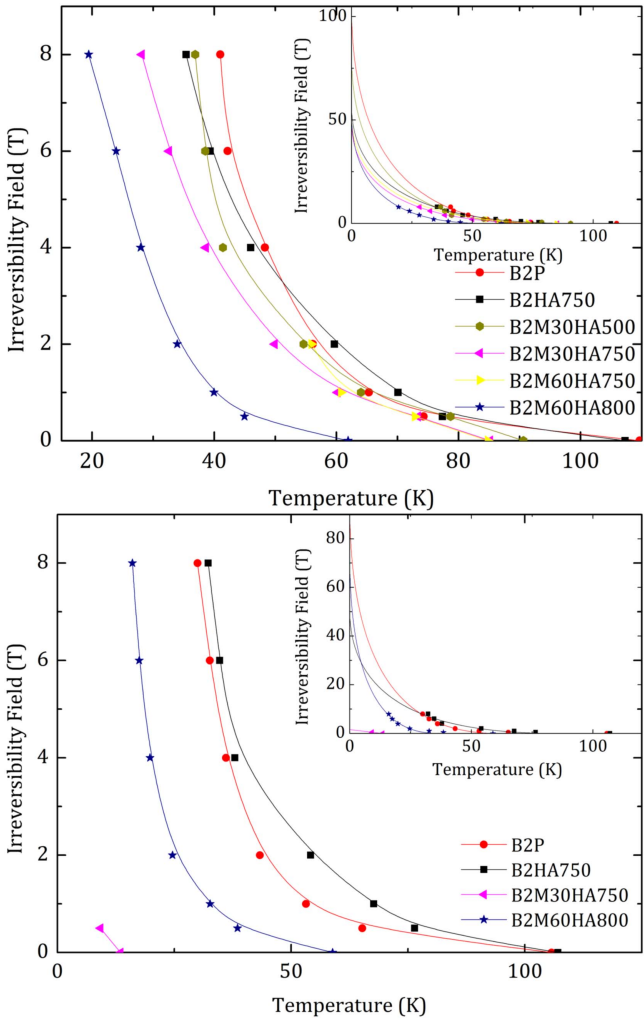


Figure 12. Irreversibility as a function of temperature of all B2 samples. (a) Small signal B_{Irr} . (b) B_{Irr} is defined as the onset in ac susceptibility measurements. The data were fitted using equation (2) or linear fits to obtain values for $B_{\text{Irr}}(0)$ as listed in table 3. Insets show the fitted curves over the full temperature range.

figure 15. However, the intergranular J_c values are still two orders of magnitude below Bi-2212 OP wires. Figure 16 shows the magnetisation J_c of B1HA750 and B1M30HA750, and compares them to the transport J_c and is discussed below in section 3.4.

Figures 17 and 18 show the hysteresis loops for B2HA750 and B2M30HA750 respectively. Similar to B1, the micro-crystalline samples show symmetric Type-II loops, while the nanocrystalline sample has asymmetric loops, except at 4.2 K, where it is symmetric. Figure 19 compares the magnetisation J_c of all B2 samples with commercial Bi-2223 tape, where the grain size was used to calculate the ntragranular J_c for all samples. Figure 20 shows the magnetisation J_c of B2HA750 and B2M30HA750, and compares them to their transport J_c .

The sequence we have chosen for field sweeping ensured we can also extract values of $\mu_0 \Delta M / \Delta B$ at -1.5 T and are listed for all our samples in table 3. Using Bean's relation for a cylinder $\Delta B = 2\mu_0 J_c R$ where ΔB is the field required to

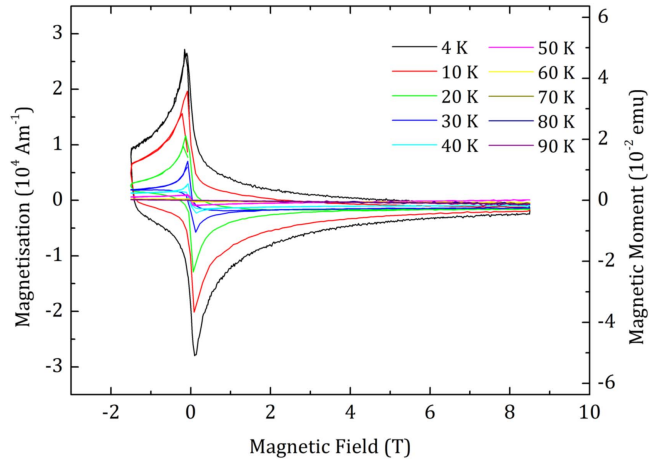


Figure 13. Magnetisation as a function of field of the B1HA750 sample between -1.5 and 8 T at temperatures between 4 and 90 K. The data at -1.5 T have a gradient $\mu_0 \Delta M / \Delta B$ of -0.2.

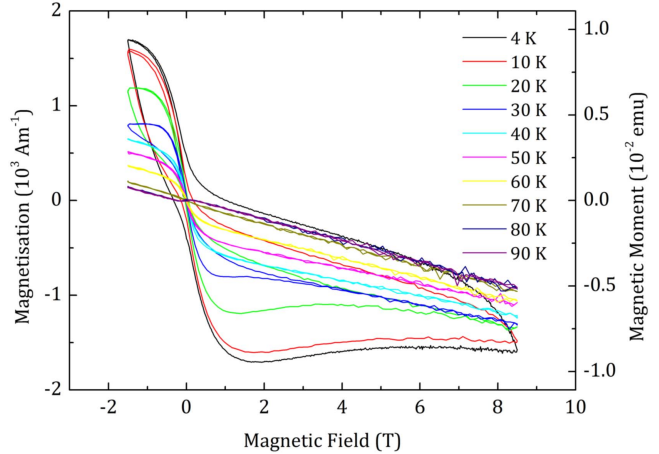


Figure 14. Magnetisation as a function of field of the B1M30HA750 sample between -1.5 and 8 T at temperatures between 4 and 90 K. The data at -1.5 T have a gradient $\mu_0 \Delta M / \Delta B$ of -3×10^{-3} .

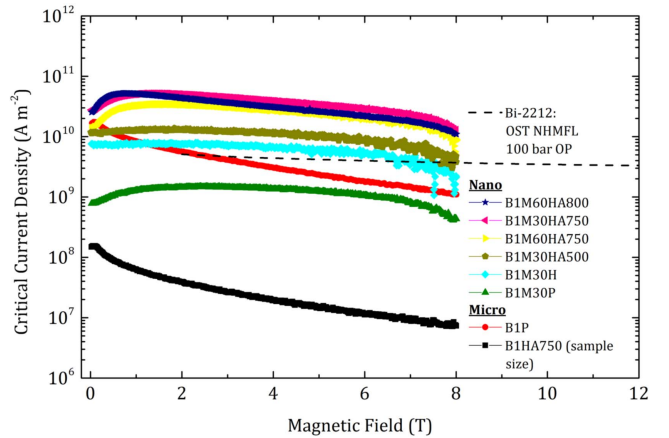


Figure 15. Magnetisation J_c as a function of field for fabricated B1 samples at 4.2 K. Grain dimensions were used to calculate magnetisation J_c , except for B1HA750, where sample dimension was used. Transport J_c of the OST NHMFL 100 bar OP sample [18] is also included for comparison.

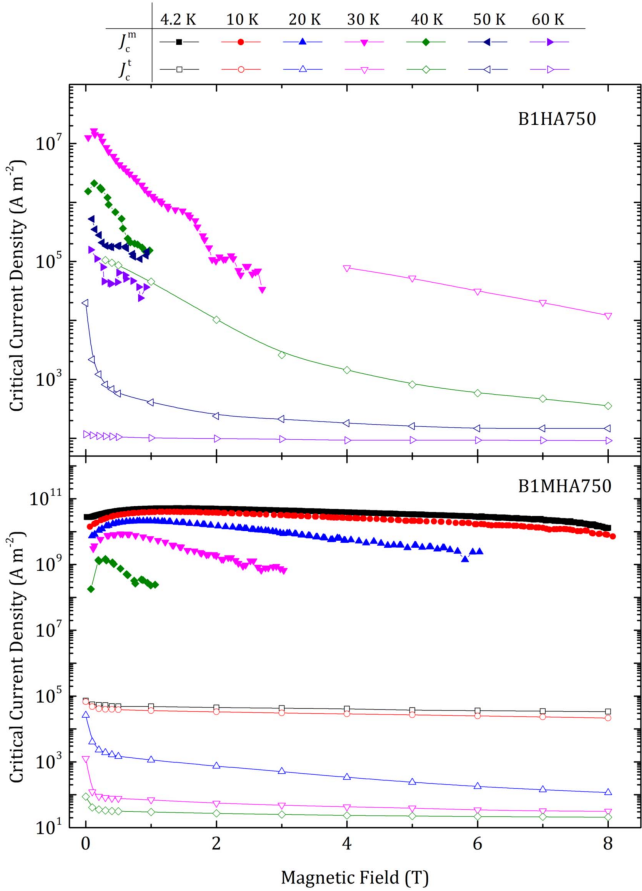


Figure 16. Transport J_c^t (open) and magnetisation J_c^m (closed) for B1 samples: Upper panel: B1HA750. At 30 K, the transport and magnetisation J_c are very similar. Lower panel: B1M30HA750.

reverse the magnetisation and equation (5) gives [54]:

$$\frac{\mu_0 \Delta M}{\Delta B} = -\frac{\frac{1}{3} J_c R}{2 J_c R} = -0.17. \quad (7)$$

Microcrystalline samples have $\mu_0 \Delta M / \Delta B$ values similar to -0.17 , which indicates that the pinning mechanism is Bean-like. However, the pressed samples remind us that this does not guarantee good connectivity between the grains. The values in nanocrystalline materials are of the order 10^{-4} – 10^{-3} . Such a decrease of $\mu_0 \Delta M / \Delta B$ has been reported in other small grained materials [55]. These values are outside the scope of Bean's model and can be indicative of surface pinning in the grains [53], consistent with the asymmetry of the hysteresis loops.

3.4. Transport critical current density measurements

After the resistivity measurements were completed in the PPMS, the PPMS circuitry was replaced with an external current supply and a multimeter for high precision four-terminal V – I measurements. The current was supplied by a Keithley 220 programmable current source. A resistor was added in series to the sample in order to confirm that the current through the sample was equal to the nominal output

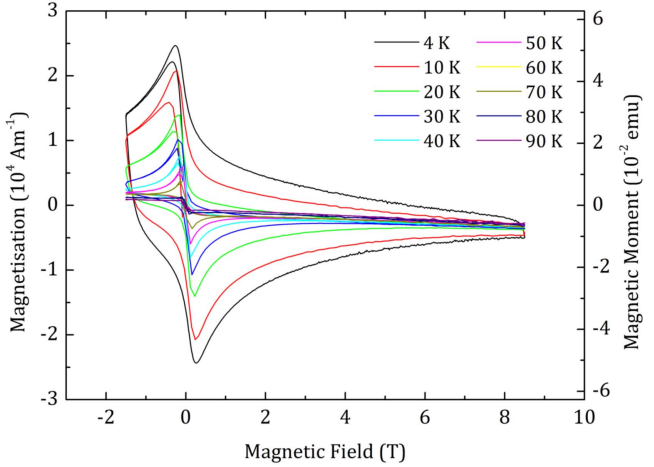


Figure 17. Magnetisation as a function of field for the B2HA750 sample between -1.5 and 8 T at temperatures between 4 and 90 K. The data at -1.5 T have a gradient $\mu_0 \Delta M / \Delta B$ of -0.1 .

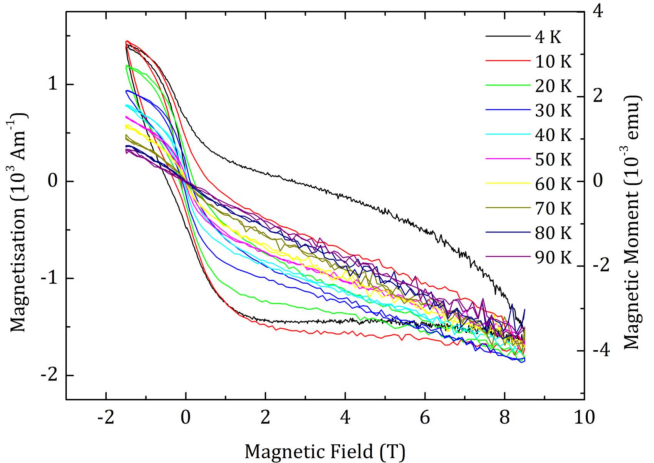


Figure 18. Magnetisation as a function of field for the B2M30HA750 sample between -1.5 and 8 T at temperatures between 4 and 90 K. The data at -1.5 T have a gradient $\mu_0 \Delta M / \Delta B$ of -3×10^{-3} .

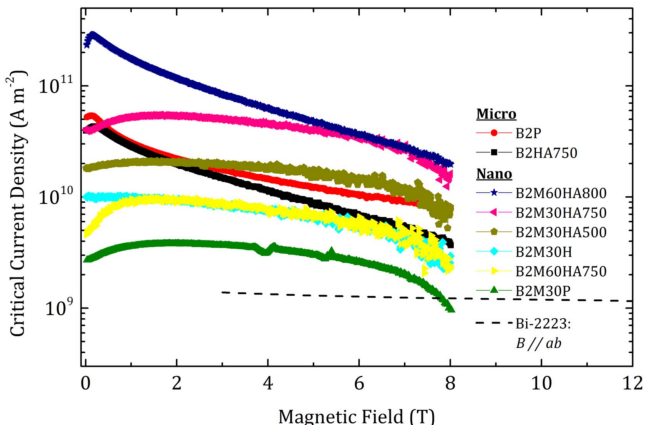


Figure 19. Magnetisation J_c as a function of field for fabricated B2 samples at 4.2 K (unless otherwise labelled). Grain size was used in these calculations. Transport J_c of Bi-2223 tape with field applied along the ab -plane is also included for comparison [18].

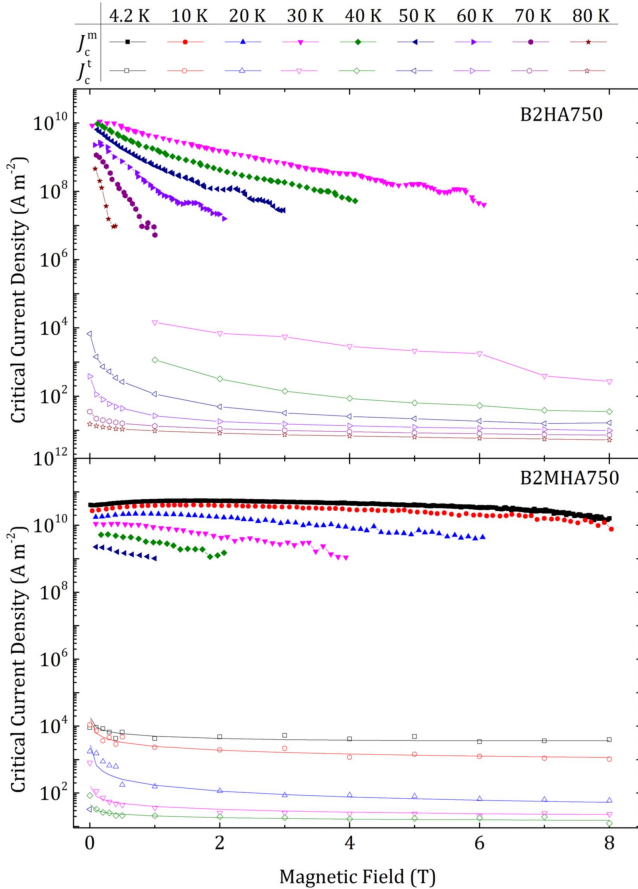


Figure 20. Transport J_c^t (open) and magnetisation J_c^m (closed) for B2 samples. Grain dimensions were used to calculate magnetisation J_c^m . Upper panel: B2HA750. Lower panel: B2M30HA750.

current in the range of 10 nA–0.1 A. The voltage across the sample taps was measured with a Keithley 2100 6½ digit multimeter, with an additional $\times 50\,000$ amplifier [56] when required, to measure extremely small voltages.

V – I traces of the B1HA750, B1M30HA750, B2HA750 and B2M30HA750 samples were measured. For the micro-crystalline samples, data are only available above 30 K, as the high currents required at low temperatures were above the limit of the current supply. Figure 21 shows the V – I traces for the B1M30HA750 sample. The red dashed line shows the 1 mV m^{-1} criterion used to define J_c^t . The values of J_c^t obtained are given in the lower panel of figure 16. The equivalent transport J_c^t data for B1HA750, B2HA750 and B2M30HA750 are given in the upper panel of figure 16 and the two panels of figure 20. We note that there is a large decrease in the transport J_c^t for the B1M30HA750 and B2M30HA750 samples, when temperature is increased from 10 to 20 K that is discussed in section 5. Most importantly the transport J_c^t in B1HA750 is typically two orders of magnitude higher than any of our other samples and in fact at 30 K is similar to the magnetisation J_c^m . For all other materials, the magnetisation J_c^m is several orders of magnitude larger than transport J_c^t and this difference remains at least two orders of magnitude, regardless of whether we use the grain or sample

dimensions to calculate J_c^m , i.e. the transport current contribution to the magnetisation is less than 1%.

4. Theoretical considerations

4.1. The resistivity of the grain boundaries

In this section, we present a method to calculate the grain boundary resistivity using polycrystalline bulk resistivity data, and single-crystal resistivity as shown in figure 5. In table 4, we have listed the single-crystal resistivity values of $\text{Bi}_2\text{Sr}_2\text{CaCu}_2\text{O}_8$ and $\text{Bi}_2\text{Sr}_2\text{Ca}_2\text{Cu}_3\text{O}_{10}$. Because of the very large $\rho_c/\rho_{ab} > 10^4$ [41, 42] and the evidence that these materials are strongly layered [13, 17, 57], we have chosen to set aside the anisotropic mass description for the angular dependence of resistivity and consider these Bi-based materials as consisting of highly conductive ab -layers separated by highly resistive layers. This leads to an angular dependence for the resistivity given by [58]

$$\rho_N(\theta) = \frac{\rho_{ab}\rho_c}{\rho_{ab}\cos^2\theta + \rho_c\sin^2\theta}. \quad (8)$$

This equation was developed by Nagata and Nakajima [58] because in two dimensional layered materials, the angular averaged resistivity in polycrystalline materials tends to be similar to the resistivity along the ab -plane, a result which cannot be explained by the anisotropic mass model. Assuming perfectly transparent grain boundaries, the theoretical angular averaged resistivity due to a collection of randomly oriented grains is then given by [58]

$$\langle \rho_N \rangle = \frac{1}{2} \int_0^\pi \rho_N(\theta) \sin \theta \, d\theta = \frac{\rho_{ab}\rho_c}{\sqrt{1 - \frac{\rho_{ab}}{\rho_c}}} \times \ln \sqrt{\frac{\rho_c}{\rho_{ab}}} \left(1 + \sqrt{1 - \frac{\rho_{ab}}{\rho_c}} \right). \quad (9)$$

The angular averaged resistivity of the grains has been calculated using the temperature dependence of the single-crystal data and is shown in figure 5. We note that had we used the anisotropic mass model, the resistivity of all B1 and B2 samples would be several orders of magnitudes below $\langle \rho_N \rangle$, which is unphysical. The grain boundary resistivity was then calculated by subtracting $\langle \rho_N \rangle$ from the measured resistivity to obtain the contribution to the total resistivity from grain boundaries only ($\Delta\rho$). This contribution ($\Delta\rho$) is then multiplied by the ratio of grain size (5 μm for micro-, 200 nm for nanocrystalline samples) to grain boundary thickness to obtain an estimate of the local resistivity of each grain boundary. Equally, we can calculate the contact (areal) resistivity by multiplying $\Delta\rho$ by the grain size. In this paper, we have assumed grain boundary thicknesses are 1 nm to enable comparisons between areal and bulk resistivity values.

For B1HA750, $J_c^m \approx J_c^t$ as shown in figure 16, and $\langle \rho_N \rangle$ is similar to the measured resistivity. Thus, our most striking result is that for the B1HA750 sample alone, the grain

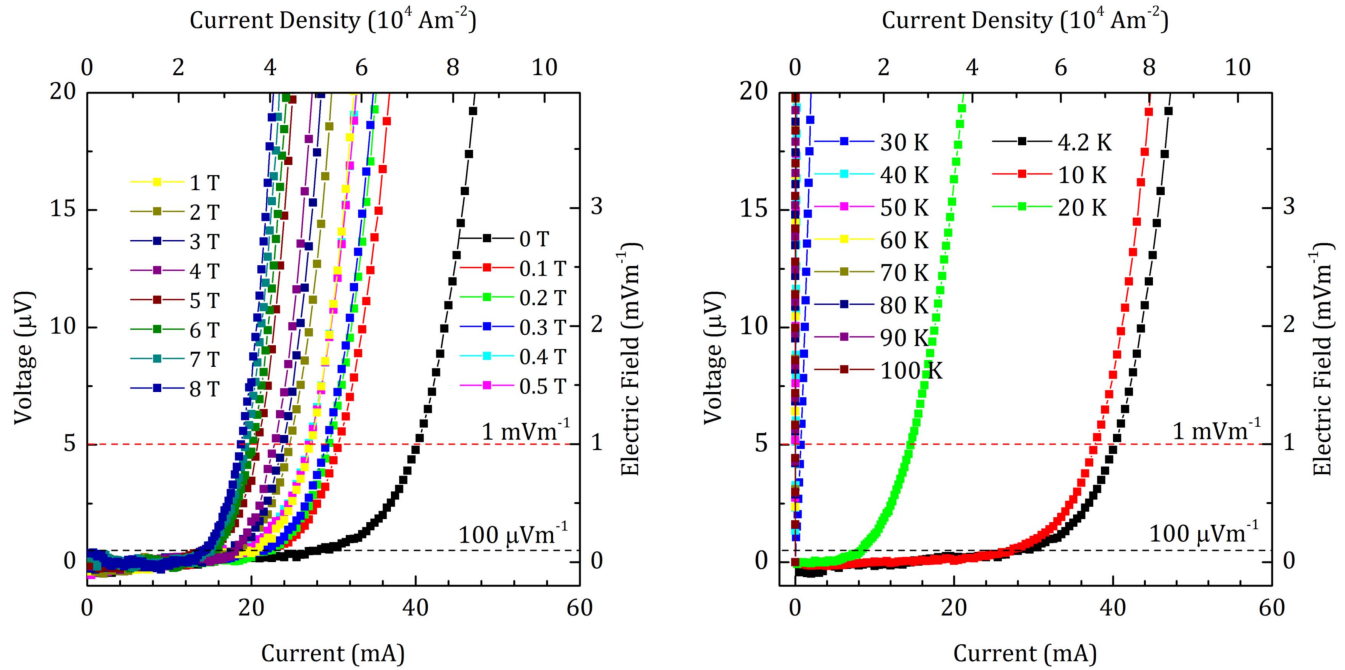


Figure 21. Left: voltage as a function of current for the B1M30HA750 sample at 4.2 K. The dashed lines show the field criteria of 1 mV m^{-1} and $100 \mu\text{V m}^{-1}$. Right: voltage as a function of current at different temperatures in zero field.

Table 4. The parameters required to calculate the ratio of the local depairing current density across a grain boundary ($J_{DN}(4.2 \text{ K})$) to the angular average (A.A.) of depairing current density of the superconducting grains $J_{DSC}(4.2 \text{ K})$ using equation (10). The resistivity of the normal layer at T_c (ρ_N), the Sommerfeld constant (γ) and the Fermi velocity (v_F) have been used to calculate the Pippard coherence length ($\xi_{SPippard}$), and the decay length of the order parameter in the grain boundary (ξ_N) [1]. For Bi-2212 we have used $\gamma = 25.2 \text{ J m}^{-3} \text{ K}^{-2}$ [87] and $v_F = 4.50 \times 10^5 \text{ m s}^{-1}$ [88] and for Bi-2223, we have used $\gamma = 33.8 \text{ J m}^{-3} \text{ K}^{-2}$ [89] and $v_F = 0.96 \times 10^5 \text{ m s}^{-1}$ [90]. The $\xi_{B_{c2}}(0)$ coherence length has been calculated using $B_{c2}(0)$ from table 1 where $(\xi_{B_{c2}}(0)) = (\Phi_0 / 2\pi B_{c2}(0))^{\frac{1}{2}}$.

Material	$\rho_N(T_c)$ ($\Omega \text{ m}$)	$\xi_{SPippard}(0)$	$\xi_{B_{c2}}(0)$ (nm)	$\xi_N(4.2 \text{ K})$ (nm)	$\frac{J_{DN}(4.2 \text{ K})}{\langle J_{DSC}(4.2 \text{ K}) \rangle}$
Bi ₂ Sr ₂ CaCu ₂ O ₈ (<i>ab</i> -plane)	3.58×10^{-6}	2.1 1.2		14	0.21
Bi ₂ Sr ₂ CaCu ₂ O ₈ (<i>c</i> -axis)	2.90×10^{-1}	0.010 0.0042		0.049	$\sim 10^{-19}$
Bi ₂ Sr ₂ CaCu ₂ O ₈ (A.A.)	2.37×10^{-5}	0.98 0.79		5.4	0.23
B1HA750	1.55×10^{-5}	1.5 0.79		6.7	0.22
B1M30HA750	9.72×10^{-3}	1.43 0.79		0.27	10^{-5}
Bi ₂ Sr ₂ Ca ₂ Cu ₃ O ₁₀ (<i>ab</i> -plane)	1.22×10^{-6}	0.86 1.1		21	0.15
Bi ₂ Sr ₂ Ca ₂ Cu ₃ O ₁₀ (<i>c</i> -axis)	6.26×10^{-2}	0.017 0.0047		0.091	$\sim 10^{-11}$
Bi ₂ Sr ₂ Ca ₂ Cu ₃ O ₁₀ (A.A.)	7.45×10^{-6}	0.66 0.70		8.3	0.19
B2HA750	1.01	0.66 0.70		0.023	$\sim 10^{-42}$
B2M30HA750	1.65×10^{-2}	0.66 0.70		0.18	$\sim 10^{-7}$

boundaries have a similar resistivity to the grains: $\rho_{GB} = \rho_S = 1.55 \times 10^{-5} \Omega \text{ m}$. For B1M30HA750, the grain boundary resistivity is $\rho_{GB} = 9.71 \times 10^{-3} \Omega \text{ m}$. These values are almost a thousand times larger than microcrystalline

values, but are nevertheless similar to Mayer's [59] grain boundary values of $(2.0\text{--}6.5) \times 10^{-3} \Omega \text{ m}$ on Bi-2212 bicrystals. For the B2 samples, the grain boundary resistivity in all our samples are large. For B2HA750, $\rho_{GB} = 1.01 \Omega \text{ m}$,

which is nearly 10^5 times large than equivalent numbers for B1HA750 and much higher than the bicrystal values of $(3.6\text{--}4.0) \times 10^{-3} \Omega\text{m}$, reported by Frey *et al* [60] and Ohbayashi *et al* [61]. B2M30HA750 has $\rho_{\text{GB}} = 1.65 \times 10^{-2} \Omega\text{m}$, which is 10^2 times lower than microcrystalline B2HA750. Given the XRD, DSC and resistivity data for B2HA750, we attribute the value to some second phase $\text{Bi}_2\text{Sr}_2\text{CaCu}_2\text{O}_8$ appearing in the grain boundaries. The grain boundary resistivities can be found in table 4.

4.2. Depairing current density of the grain boundaries

In this section we follow the approach we used for YBCO [1] to calculate the local depairing current density across a normal (i.e. non-superconducting) grain boundary (J_{DN}). If the transport current through a grain boundary is modelled as a 1D S-N-S junction, the analytic solution to the Ginzburg–Landau equations in zero field is given by [12]:

$$J_{\text{DN}}(T) \approx J_{\text{DSc}}(T) \sqrt{2} \frac{\rho_S \xi_S}{\rho_N \xi_N} \left\{ \sqrt{\left(\frac{\xi_S \rho_S}{\xi_N \rho_N \sqrt{2}} \right)^2 + 1} - \frac{\xi_S \rho_S}{\xi_N \rho_N \sqrt{2}} \right\}^2 \exp\left(\frac{-2d}{\xi_N}\right), \quad (10)$$

where $J_{\text{DSc}}(T)$ is the depairing current density in the superconducting grain, ρ_S/ρ_N is the ratio of the resistivity in the grain to the grain boundary, ξ_S/ξ_N is the ratio of the G–L coherence length in the superconductor to the decay length of the order parameter across the grain boundary, and d is the thickness of the grain boundary. In order to simplify the calculations, we have assumed the grain boundary T_c to be 0 K. We can expect this to break down in the case of very low-angle grain boundaries where the grain boundaries themselves may be considered as strained superconductors. We have also made the simplifying assumptions that we can use angular averages for each of the parameters and ignore the complexity associated with grains with different critical properties (with respect to the direction of current flow) on either side of a given grain boundary as well as percolation. In table 4, we provide calculations of $J_{\text{DN}}(T)$ at 4.2 K for both $\text{Bi}_2\text{Sr}_2\text{CaCu}_2\text{O}_8$ and $\text{Bi}_2\text{Sr}_2\text{Ca}_2\text{Cu}_3\text{O}_{10}$, along the ab -plane, and in the c -axis direction. All angular averaged values of $J_{\text{DN}}(T)$ in table 4 were calculated using relevant resistivity values in equation (10). For the ab -plane and c -axis data, the grains and the grain boundaries were assumed to have the same resistivity, $\rho_N = \rho_S$, where ρ_S is simply the single-crystal resistivity values from the literature. The angular averaged resistivity (A.A.) is calculated from the single-crystal values. For the HA750 samples and the M30HA750 samples, we have assumed the resistivity of the grains is that calculated for the A.A. sample. The values of $\rho_N(T_c)$, the resistivity of the normal layer at T_c for each material considered, used in equation (10) are listed in table 4. The superconductor layer coherence length ξ_S used in equation (10) was calculated at 4.2 K following the approach used in table 1. $\xi_{\text{SPippard}}(0)$ is the Pippard coherence length calculated from the Fermi velocity (v_F), resistivity (ρ_S), and

the Sommerfeld constant (γ). $\xi_{B_{c2}}(0)$ is the superconductor coherence length calculated naively from $B_{c2}(0)$. We have produced the different angular averaged coherence lengths, $\xi_{\text{SPippard}}(0)$ and $\xi_{B_{c2}}(0)$ so we could check that they have similar values and hence have confidence that the microscopic values used to calculate $\xi_N(4.2 \text{ K})$ [1, 12] and J_{DN} are reasonable.

Table 4 shows, for both $\text{Bi}_2\text{Sr}_2\text{CaCu}_2\text{O}_8$ and $\text{Bi}_2\text{Sr}_2\text{Ca}_2\text{Cu}_3\text{O}_{10}$, the single-crystal values of $J_{\text{DN}}/\langle J_{\text{DSc}} \rangle$ along the ab -plane are near 0.2, whereas $J_{\text{DN}}/\langle J_{\text{DSc}} \rangle$ in the c -axis direction is more than 10 orders of magnitude smaller. The angular averaged $J_{\text{DN}}/\langle J_{\text{DSc}} \rangle$ are of the order of 0.2, consistent with most current transport occurring along the ab -plane. The values quoted in table 4 that were derived using angular averages have larger uncertainties, associated with the simplifications we have made. Given the high resistivity anisotropy, it is reasonable to assume that $J_{\text{DN}}/\langle J_{\text{DSc}} \rangle$ of the theoretical angular average material is similar to that along the ab -plane. One of the important result in this paper is that the B1HA750 sample has a low grain boundary resistivity and a value for $J_{\text{DN}}/\langle J_{\text{DSc}} \rangle \approx 0.22$, similar to the A.A. sample. The B1M30HA750, B2HA750 and B2M30HA750 samples have grain boundary resistivities that are so high that ξ_N decreases to below the thickness of the grain boundaries (i.e. $d = 1 \text{ nm}$), the exponential term in equation (10) dominates and $J_{\text{DN}}/\langle J_{\text{DSc}} \rangle$ is severely suppressed to the very small values shown in table 4.

5. Discussion

It is well known that grain boundaries can have very different properties to their parent crystalline material because of the redistribution of the component elements and the different structure [62, 63]. In this paper we have adopted the most straightforward description of grain boundaries, by considering them as non-superconducting resistive barriers and calculated the consequences. This ignores complexity associated with very low-angle grain boundaries, that at sufficiently low angles are probably best described as partially superconducting, and high angle grain boundaries that may even be ferromagnetic [62, 63], which in the Ginzburg–Landau framework can be described using negative local critical temperatures. DSC data show that both B1 and B2 samples, micro- or nanocrystalline, consist mainly of their nominal $\text{Bi}_2\text{Sr}_2\text{CaCu}_2\text{O}_8$ or $\text{Bi}_2\text{Sr}_2\text{Ca}_2\text{Cu}_3\text{O}_{10}$ phases. However, XRD data show that significant secondary phase signals appear after a combination of milling, HIP'ing and annealing. These latter processes were unavoidable in order to restore superconductivity to the nanocrystalline samples. We note that XRD measurements produce large peaks for ordered crystalline material and are much less sensitive to detecting amorphous or nanocrystalline phases. Hence, consistent with the lower magnitude of the signals observed for the nanocrystalline samples, the XRD data preferentially identifies ordered second phase material. In contrast, the DSC data, which shows largely Bi-based superconducting phases and relatively small amounts of second phase material, is

volumetric. We cannot rule out the possibility that the small signals that we have found at the highest temperatures and magnetic fields in the ac magnetic susceptibility data are associated with a very small fraction, a minority phase, of large grained material with optimum properties. However, we consider this unlikely since it would mean that: the milling had not produced broadly homogenised polycrystalline material with uniform nano-grain size, the weak field dependence for J_c^m consistent with strong pinning is due to this fraction and our calculations of J_c^m related to granularity associated with the magnitude of the small signals, have just by chance given values that are similar to optimum values from the literature.

We have used complementary transport and magnetic measurements to distinguish intergranular currents from intragranular, and infer the properties of the grain boundaries. For homogeneous single-crystal samples, the temperature at which the large screening signal is found (T_c^*) can be assigned to the average or characteristic critical temperature for the material. When T_c^* is lower than optimum values, it is usually associated with disorder or off-stoichiometry. However in polycrystalline samples, several interpretations for a low T_c^* arise. The grains themselves can have degraded critical properties but be connected by low resistivity grain boundaries. In these cases, T_c^* is predominantly determined by the grains. This interpretation is most often valid for polycrystalline metals and alloys where even high angle grain boundaries can have a similar resistivity to the grains [1]. At the other end of the spectrum, one can consider the grains to have good critical properties and the grain boundaries to be non-superconducting and highly resistive. The structural and compositional changes at the grain boundaries cause large changes in resistivity and T_c^* is a complex function of coupling between grains across highly resistive grain boundaries. This is more likely to occur in oxide materials produced by milling and HIPing as used in this work (see figure 8 and table 3). In this paper, we have measured the small signals that occur at high temperature and fields and associated them with isolated (non-coupled) well-ordered grains with very high critical properties. We also note that both the fundamental considerations outlined by Deutscher *et al* [64] and the empirical measurements in the literature [31, 65] suggest that at a grain size of 200 nm, the grains in our nanocrystalline samples are still large enough to have the optimum properties of bulk material.

For B1HA750, the resistivity of the grain boundaries are low, the transport and magnetisation are similar, J_c^t is $7.8 \times 10^4 \text{ A m}^{-2}$ at 4 T and 30 K, and we observed a Bean-like value for $\mu_0 \Delta M / \Delta B \approx -0.2$. These results are typical of a well-connected LTS material. Nevertheless J_c^t is about two orders of magnitude lower than J_{DN} . We note that in samples with well-connected grains, one can expect the surface pinning in the grains to be reduced. We interpret our data and theoretical considerations as evidence that this sample has well-connected grains that could carry critical current densities up to 20% of J_{DSC} but that weak pinning is the limiting factor for the suppression of J_c . The low J_c^t values are

consistent with the large grains (D) [66, 67] and the large Ginzburg–Landau parameter (κ) values of B1HA750 since for grain boundary pinning $J_c \propto 1/D\kappa^2$ [68]. Unfortunately, unlike LTS, we have found in nanocrystalline materials that reducing the grain size decreased J_c^t in Bi-materials because the grain boundaries become highly resistive. We suggest a different approach to increasing pinning in polycrystalline $\text{Bi}_2\text{Sr}_2\text{CaCu}_2\text{O}_8$, following the approach of 2 G YBCO tapes and single-crystal Nb films [1], namely increasing pinning by adding artificial pinning sites or perhaps using irradiation. The pinning sites would need to provide energy wells for the fluxons that are significantly deeper than the grain boundaries. Kumakura *et al* [69, 70] reported irradiated Nb_3Al tape with increased $J_c = 2 \times 10^8 \text{ A m}^{-2}$ at 23 T and 4.2 K. Proton irradiation of MgB_2 by Bugoslavsky *et al* [71] and neutron irradiation of A15 materials by Bauer *et al* [72] also showed an enhancement in pinning and increase in J_c . However, the results reported in the literature can be mixed, depending on the irradiation particle, energy, duration and type of defects created. Nishimura *et al* [73] found neutron irradiation increased J_c in Nb_3Sn at low fields, but had no effect on $\text{Nb}-\text{Ti}$ and Nb_3Al wires, or on $\text{Bi}_2\text{Sr}_2\text{Ca}_2\text{Cu}_3\text{O}_{10}$ tapes. An improvement in flux pinning was seen in proton irradiated sintered ceramic pellets of YBCO and $\text{Bi}_2\text{Sr}_2\text{Ca}_2\text{Cu}_3\text{O}_{10}$ by Mezzetti *et al* [74], and in ion irradiated melt-textured YBCO with a high concentration of discontinuous columnar defects by Fuchs *et al* [75]. However, Behera *et al* [76] found that swift heavy ion irradiation of YBCO granular thick films damaged grain boundaries, and Eisterer *et al* [77] found that neutron irradiation of YBCO coated conductors found no improvements. Irradiation is a promising route but the parameter space is vast and systematic studies with good information about values of J_{DN} and J_{PN} will be required to optimise J_c .

For the B1M30HA750 sample, the resistivity of the grain boundaries is high, $\rho_N(T_c) = 9.30 \times 10^{-3} \Omega\text{m}$, consistent with literature bicrystal values [59], $J_c^t \ll J_c^m$, and the values of $\mu_0 \Delta M / \Delta B$ are small. We note that the grain boundary resistivity is much higher than the microcrystalline counterpart. J_{DN} is five orders of magnitude below J_{DSC} . Poor pinning can cause transport J_c^t across the grain boundaries to decrease even further, and the measured J_c^t is another factor of 30 below J_{DN} . However, the literature for $\text{Bi}_2\text{Sr}_2\text{CaCu}_2\text{O}_8$ bicrystals gives grain boundary resistivities of $(2\text{--}6.5) \times 10^{-3} \text{ A m}^{-2}$ with transport critical current densities of $J_c^{GB}(0 \text{ T}, 4.2 \text{ K}) = (0.2\text{--}1.5) \times 10^8 \text{ A m}^{-2}$ [59]. This is consistent with J_{DN} calculated using equation (10), and shows that it is possible to increase pinning across grain boundaries. We attribute the large decrease in J_c^t between 10 and 20 K (not observed in the J_c^m magnetic measurements) either to large reduction in the irreversibility field in this temperature range or to regions near the grain boundaries becoming superconducting below 20 K (possibly associated with $\text{Bi}_2\text{Sr}_2\text{CuO}_6$ at the grain boundaries), evidenced by the field dependence of resistivity, initially increasing as temperature drops below T_c , then decreasing as the temperature approaches 20 K, as well as the rapid increase in screening shown in the ac magnetic susceptibility data. We do not know whether or

not formation of $\text{Bi}_2\text{Sr}_2\text{CuO}_6$ at the grain boundaries can be avoided using variants of the fabrication routes in this work. Nevertheless, at 4.2 K when one may expect $\text{Bi}_2\text{Sr}_2\text{CuO}_6$ to be superconducting, the transport J_c values are a similar order of magnitude to those at and above 20 K which suggests the $\text{Bi}_2\text{Sr}_2\text{CuO}_6$ does not significantly affect the conclusions of this work. The magnetisation J_c^m is high in this material, associated with high intragranular current densities. We consider this sample to be a collection of high quality grains that are poorly connected.

For the B2HA750 sample, the angular average grain boundary resistivity is $1.01 \Omega\text{m}$, even higher than the resistivity in the c -axis direction of single-crystal $\text{Bi}_2\text{Sr}_2\text{Ca}_2\text{Cu}_3\text{O}_{10}$. Without considering pinning, the high grain boundary resistivities alone is enough to cause J_{DN} to be very small as seen in table 4, and is the limiting factor for the suppression of J_c . The measured, non-zero J_c^t is likely due to the existence of a percolative path. Again, we consider this sample to be high quality grains separated by highly resistive grain boundaries.

B2M30HA750 has an extremely high grain boundary resistivity of $1.65 \times 10^{-2} \Omega\text{m}$, much higher than literature bicrystal values on the order of $10^{-3} \Omega\text{m}$ [60, 61]. $J_c^t \ll J_c^m$, and the values of $\mu_0 \Delta M / \Delta B$ are small. The measured $J_c^t(0 \text{ T}, 4.2 \text{ K}) = 9.1 \times 10^3 \text{ A m}^{-2}$, an order of magnitude below J_{DN} , thus the limiting factor for the suppression of J_c is due to the high grain boundary resistivity. Similar to B1M30HA750, there is the large decrease in J_c^t between 10 and 20 K. We consider the B2M30HA750 sample to be similar to the B1M30HA750 sample and as such to be a highly granular sample.

Unlike $\text{YBa}_2\text{Cu}_3\text{O}_7$ [78], there are no detailed measurements of the angular dependence of the resistivity ($\rho_N(\theta)$), for either $\text{Bi}_2\text{Sr}_2\text{CaCu}_2\text{O}_8$ or $\text{Bi}_2\text{Sr}_2\text{Ca}_2\text{Cu}_3\text{O}_{10}$ single crystals, thus we have estimated the angular averaged resistivity of the grains using a layered model (see section 4.1). This led to a grain boundary resistivity that is a lower limit for B1HA750. Detailed single-crystal data for $\rho_N(\theta)$, together with detailed measurements and analysis of XRD data that provide the degree of texturing, would allow us to distinguish more accurately the role of the texturing in these samples and provide more accurate values of the grain boundary depairing current density. The very limited literature on high angle grain boundaries also prevents us from assessing whether the angular averaged values calculated and measured in this work can be considered typical or intrinsic. Much more work is needed before one can make general statements about grain boundaries and how effective grain boundary engineering may be in manipulating their properties. Among our materials, microcrystalline $\text{Bi}_2\text{Sr}_2\text{CaCu}_2\text{O}_8$ is the only material for which grain boundary engineering could yet produce useful commercial materials, when combined with improvements in pinning. For nanocrystalline B1 and micro- or nanocrystalline B2, reducing the grain boundary resistivity or removing the grain boundaries altogether, is a prerequisite for improving J_c .

6. Conclusion

Both micro- and nanocrystalline $\text{Bi}_2\text{Sr}_2\text{CaCu}_2\text{O}_8$ and $\text{Bi}_2\text{Sr}_2\text{Ca}_2\text{Cu}_3\text{O}_{10}$ samples were fabricated and measured. A complementary set of dc magnetisation, ac magnetic susceptibility and transport measurements allowed us to distinguish intergranular currents from intragranular currents. We have calculated the grain boundary resistivity for these materials and combined this with the 1D S-N-S junction model for polycrystalline materials to calculate the suppression of J_c due to grain boundaries. The most interesting sample we have studied is polycrystalline $\text{Bi}_2\text{Sr}_2\text{CaCu}_2\text{O}_8$ with grain sizes on the order of microns. Whilst grain boundary resistivity does decrease the local depairing current density by an order of magnitude, this sample alone has the potential for very high J_c if strong pinning centres can be introduced. The theoretical calculations for $\text{Bi}_2\text{Sr}_2\text{CaCu}_2\text{O}_8$ and $\text{Bi}_2\text{Sr}_2\text{Ca}_2\text{Cu}_3\text{O}_{10}$ have similarities with other commercial superconductors including YBCO, LTS and Fe-based superconductors, in that there is an intrinsic loss in depairing current density by about a factor of five simply by the presence of grain boundaries in polycrystalline materials. Furthermore, the materials with the highest J_c/J_{DSC} [1], whether it is the cuprate material YBCO [18], Fe-based material $\text{Ba}(\text{FeCo})_2\text{As}_2$ [79] or the elemental material Nb [80], are tapes with no large angle grain boundaries and strong pinning. The materials with the lowest J_c/J_{DSC} are polycrystalline materials, including MgB_2 [81] and A15 materials [66, 67, 82, 83]. Although removing high angle grain boundaries from technological polycrystalline materials is the favoured route to increase J_c , so far, this approach has proven very expensive. We suggest that cost constraints may yet lead to use of broadly untextured polycrystalline $\text{Bi}_2\text{Sr}_2\text{CaCu}_2\text{O}_8$ materials, with artificial pinning sites or perhaps pinning produced by irradiation, that have high J_c .

Acknowledgments

The authors would like to thank the members of the Durham Superconductivity Group, the Durham mechanical workshop and in particular Steve Lishman, as well as Mr Mike Glynn and Professor Moataz Attallah at Birmingham University for their support and use of their HIP facilities. The data are available at: <https://doi.org/10.15128/r1nz805z69x> and associated materials are on the Durham Research Online website: <http://dro.dur.ac.uk/>. This work is funded by EPSRC grant EP/K502832/1 and the EPSRC grant EP/L01663X/1 for the Fusion Doctoral Training Network.

ORCID iDs

Damian P Hampshire  <https://orcid.org/0000-0001-8552-8514>

References

- [1] Wang G, Raine M J and Hampshire D P 2017 How resistive must grain-boundaries be to limit J_c in polycrystalline superconductors? *Supercond. Sci. Technol.* **30** 104001
- [2] Schauer W and Schelb W 1981 Improvement of Nb_3Sn high field critical current by a two-stage reaction *IEEE Trans. Magn.* **17** 374–7
- [3] Carty G J and Hampshire D P 2008 Visualising the mechanism that determines the critical current density in polycrystalline superconductors using time-dependent Ginzburg–Landau theory *Phys. Rev. B* **77** 172501
- [4] Gutierrez J et al 2007 Strong isotropic flux pinning in solution-derived $\text{YBa}_2\text{Cu}_3\text{O}_{7-x}$ nanocomposite superconductor films *Nat. Mater.* **6** 367–73
- [5] Dimos D, Chaudhari P and Mannhart J 1990 Superconducting transport properties of grain boundaries in $\text{YBa}_2\text{Cu}_3\text{O}_7$ bicrystals *Phys. Rev. B* **41** 4038–49
- [6] Amrein T, Schultz L, Kabius B and Urban K 1995 Orientation dependence of grain-boundary critical current densities in high- T_c bicrystals *Phys. Rev. B* **51** 6792
- [7] Attenberger A, Hanisch J, Holzapfel B and Schultz L 2002 Electrical transport properties of Bi2223 [001] tilt grain boundary junctions *Physica C* **372–376** 649–51
- [8] Vodolazov D Y 2000 Effect of surface defects on the first field for vortex entry in type-II superconductors *Phys. Rev. B* **62** 8691–4
- [9] Carty G J, Machida M and Hampshire D P 2005 Numerical studies on the effect of normal metal coatings on the magnetisation characteristics of type-II superconductors *Phys. Rev. B* **71** 144507
- [10] Lee T S, Jenkins I, Surrey E and Hampshire D P 2015 Optimal design of a toroidal field magnet system and cost of electricity implications for a tokamak using high temperature superconductors *Fusion Eng. Des.* **98–99** 1072–5
- [11] Tsui Y, Surrey E and Hampshire D P 2016 Soldered joints—an essential component of demountable high temperature superconducting fusion magnets *Supercond. Sci. Technol.* **29** 075005
- [12] Carty G J and Hampshire D P 2013 The critical current density of an SNS junction in high magnetic fields *Supercond. Sci. Technol.* **26** 065007
- [13] Clem J R 1991 Two-dimensional vortices in a stack of thin superconducting films: a model for high-temperature superconducting multilayers *Phys. Rev. B* **43** 7837–46
- [14] Chen B et al 2007 Two-dimensional vortices in superconductors *Nat. Phys.* **3** 239–42
- [15] Blatter G, Feigelman M V, Geshkenbein V B, Larkin A I and Vinokur V M 1994 Vortices in high-temperature superconductors *Rev. Mod. Phys.* **66** 1125–388
- [16] Piriou A, Fasano Y, Giannini E and Fischer Ø 2007 Doping-dependence of the vortex phase diagram of $\text{Bi}_2\text{Sr}_2\text{Ca}_2\text{Cu}_3\text{O}_{10+\delta}$ *Physica C* **460** 408–9
- [17] Senator C 2016 30 years to HTS—Status and Perspectives
- [18] Larbalestier D C et al 2014 Isotropic round-wire multifilament cuprate superconductor for generation of magnetic fields above 30 T *Nat. Mater.* **13** 375–81
- [19] Kametani F, Jiang J, Matras M, Abraimov D, Hellstrom E E and Larbalestier D C 2015 Comparison of growth texture in round Bi2212 and flat Bi2223 wires and its relation to high critical current density development *Sci. Rep.* **5** 8285
- [20] Ando Y et al 1999 Resistive upper critical fields and irreversibility lines of optimally doped high- T_c cuprates *Phys. Rev. B* **60** 12475–9
- [21] Beille J et al 1988 Pressure effects, anisotropic transport properties and upper critical fields of $\text{Bi}_2\text{Sr}_2\text{CaCu}_2\text{O}_{8+x}$ single crystals—characterization of needle-like Bi–Sr–Ca–Cu–O crystals *Physica C* **156** 448–54
- [22] Yildirim G, Varilci A and Terzioglu C 2013 Anisotropic nature and scaling of thermally activated dissipation mechanism in Bi-2223 superconducting thin film *J. Alloys Compd.* **554** 327–34
- [23] Hensel B, Grasso G and Flükiger R 1995 Limits to the critical transport current in superconducting $(\text{Bi},\text{Pb})\text{Sr}_2\text{Ca}_2\text{Cu}_3\text{O}_{10}$ silver-sheathed tapes: the railway-switch model *Phys. Rev. B* **51** 15456–73
- [24] Heine K, Tenbrink J and Thoner M 1989 High-field critical current densities in $\text{Bi}_2\text{Sr}_2\text{Ca}_1\text{Cu}_2\text{O}_{8+x}/\text{Ag}$ wires *Appl. Phys. Lett.* **55** 2441–3
- [25] Noritsugu E, Hiroyuki K, Naoki U, Hiroaki K, Kazumasa T and Kazuo W 1990 The high field magnetic dependence of critical current density at 4.2 K for Ag-sheathed $\text{Bi}_2\text{Sr}_2\text{CaCu}_2\text{O}_y$ superconducting tape *Japan. J. Appl. Phys.* **29** L447
- [26] Hikata T, Sato K and Hitotsuyanagi H 1989 Ag-sheathed Bi–Pb–Sr–Ca–Cu–O superconducting wires with high critical current density *Japan. J. Appl. Phys.* **28** 82
- [27] Osamura K et al 2009 Improvement of reversible strain limit for critical current of Bi-SCCO due to lamination technique *IEEE Trans. Appl. Supercond.* **19** 3026–9
- [28] Osamura K, Machiya S and Hampshire D P Jun 2016 Mechanism for the uniaxial strain dependence of the critical current in practical REBCO tapes *Supercond. Sci. Technol.* **29** 065019
- [29] T M C Ltd Energy Device Materials—high-temperature superconducting materials <http://material-sys.com/global/content21/> (Accessed: 1 September 2017)
- [30] Oberteuffer J 1974 Magnetic separation: a review of principles, devices, and applications *IEEE Trans. Magn.* **10** 223–38
- [31] Zhao W, Jin H, Tian M, Ruan K, Yang L and Cao L 1998 Nanocrystalline-grained Bi–Sr–Ca–Cu–O and its superconducting property *Appl. Phys. A* **66** 451–4
- [32] Matheis D P, Misture S T and Snyder R L 1993 Melt-texture processing and high-temperature reactions of Bi-2212 thick films *Physica C* **217** 319–24
- [33] Przybylski K and Brylewski T 1995 The formation of superconducting oxide phases in the $(\text{Bi},\text{Pb})\text{–Sr}\text{–Ca}\text{–Cu}\text{–O}$ system *J. Therm. Anal.* **45** 1135–43
- [34] Masaaki M, Hozumi E, Jun T, Naoto K, Akihiko S and Yasuo O 1988 Superconductivity of $\text{Bi}_2\text{Sr}_2\text{Ca}_2\text{Cu}_3\text{Pb}_x\text{O}_y$ ($x = 0.2, 0.4, 0.6$) *Japan. J. Appl. Phys.* **27** L1225
- [35] Chen Y L, Stevens R, Lo W and Zhen Y S 1990 Synthesis and characterization of 110 K superconducting phase in $\text{Bi}(\text{Pb})\text{–Sr}\text{–Ca}\text{–Cu}\text{–oxide}$ *J. Mater. Sci., Mater. Electron.* **1** 185–91
- [36] Majewski P 2000 Materials aspects of the high-temperature superconductors in the system $\text{Bi}_2\text{O}_3\text{–SrO}\text{–CaO}\text{–CuO}$ *J. Mater. Res.* **15** 854–70
- [37] Schwarz R B and Petrich R R 1988 Calorimetry study of the synthesis of amorphous Ni–Ti alloys by mechanical alloying *J. Less-Common Met.* **140** 171
- [38] Taylor D M J, Al-Jawad M and Hampshire D P 2008 A new paradigm for fabricating bulk high-field superconductors *Supercond. Sci. Technol.* **21** 125006
- [39] Niu H J and Hampshire D P 2003 Disordered nanocrystalline superconducting PbMo_6S_8 with very large upper critical field *Phys. Rev. Lett.* **91** 027002
- [40] Quantum Design 2004 PPMS resistivity option user's manual *PPMS Hardware and Options Manual* (San Diego: Quantum Design)
- [41] Chen X H et al 1998 Anisotropic resistivities of single-crystal $\text{Bi}_2\text{Sr}_2\text{CaCu}_2\text{O}_{8+d}$ with different oxygen content *Phys. Rev. B* **58** 14219–22
- [42] Fujii T, Watanabe T and Matsuda A 2001 Comparative study of transport properties of $\text{Bi}_2\text{Sr}_2\text{Ca}_2\text{Cu}_3\text{O}_{10+\delta}$ and $\text{Bi}_2\text{Sr}_2\text{CaCu}_2\text{O}_{8+d}$ single crystals *Physica C* **357–360** 173–6

- [43] Naruaki T, Yutaka T, Minoru M and Yoichi I 1992 The superconducting properties of [001] twist boundaries in a Bi-Sr-Ca-Cu-O superconductor *Japan. J. Appl. Phys.* **31** L942
- [44] Dogrue M, Zalaoglu Y, Varilci A, Terzioglu C, Yildirim G and Ozturk O 2012 A study on magnetoresistivity, activation energy, irreversibility and upper critical field of slightly Mn added Bi-2223 superconductor ceramics *J. Supercond. Novel Magn.* **25** 961–8
- [45] Quantum Design 2004 PPMS ACMS user's manual *PPMS Hardware and Options Manual* (San Diego: Quantum Design) pp 1–3
- [46] Gomathi A, Sundaresan A and Rao C N R 2007 Room-temperature ferromagnetism in nanoparticles of superconducting materials *Solid State Commun.* **142** 685–8
- [47] Hasanain S K, Akhtar N and Mumtaz A 2011 Particle size dependence of the superconductivity and ferromagnetism in YBCO nanoparticles *J. Nanopart. Res.* **13** 1953–60
- [48] Pusceddu E and Hampshire D P 2012 Nanocrystalline superconducting islands of Nb₃Ge in a resistive grain boundary matrix with a bulk critical temperature of 12 K *Supercond. Sci. Technol.* **25** 115014
- [49] Shoenberg D 1952 *Superconductivity*. (Cambridge: Cambridge University Press)
- [50] Sunwong P, Higgins J S, Tsui Y, Raine M J and Hampshire D P 2013 The critical current density of grain boundary channels in polycrystalline HTS and LTS superconductors in magnetic fields *Supercond. Sci. Technol.* **26** 095006
- [51] Bean C P 1964 Magnetization of high-field superconductors *Rev. Mod. Phys.* **36** 31–9
- [52] Poole C P, Farach H A and Creswick R J 1995 *Superconductivity*. (San Diego, CA: Academic Press)
- [53] Carr W J and Wagner G R 1986 Surface current and hysteresis in fine filament NbTi superconductors *J. Appl. Phys.* **60** 342–5
- [54] Campbell A M 1969 The response of pinned flux vortices to low-frequency fields *J. Phys. C: Solid State Phys.* **2** 1492–501
- [55] Shimizu E and Ito D 1989 Critical current density obtained from particle-size dependence of magnetization in YBa₂Cu₃O_{7-δ} powders *Phys. Rev. B* **39** 2921–3
- [56] EM Electronics DC Nanovolt Amplifier Model A10, <http://emelectronics.co.uk/a10.html> (Accessed: 19 September 2016)
- [57] Laguna M F, Domínguez D and Balseiro C A 2000 Transport properties and structures of vortex matter in layered superconductors *Phys. Rev. B* **62** 6692–8
- [58] Nagata S and Nakajima M 1993 Averaging effect of the anisotropy of the electrical resistivity in a polycrystalline sample *Physica B* **192** 228
- [59] Mayer B, Alff L, Trguble T and Gross R 1993 Superconducting transport properties of Bi₂Sr₂CaCu₂O_{8+x} bicrystal grain boundary junctions *Appl. Phys. Lett.* **63** 996–8
- [60] Frey U, Meffert H, Haibach P, Üstüner K, Jakob G and Adrian H 1996 Transport properties of Bi₂Sr₂Ca₂Cu₃O_{10+d} bicrystal grain boundary Josephson junctions and SQUIDS *J. Physique IV* **06** C3-277–282
- [61] Ohbayashi K et al 1995 Fabrication of Bi₂Sr₂Ca₂Cu₃O_x thin film grain boundary junctions *IEEE Trans. Appl. Supercond.* **5** 2816–9
- [62] Straumal B B et al 2015 Grain boundaries as a source of ferromagnetism and increased solubility of Ni in nanograined ZnO *Rev. Adv. Mater. Sci.* **41** 61–71
- [63] Straumal B B et al 2016 Ferromagnetic behaviour of ZnO: the role of grain boundaries *Beilstein J. Nanotechnol.* **7** 1936–47
- [64] Bennemann K H and Ketterson J B 2004 *The Physics of Superconductors: Vol. II: Superconductivity in Nanostructures, High-Tc And Novel Superconductors, Organic Superconductors* (Berlin: Springer)
- [65] Jin H et al 1997 Correlation of grain size and ac susceptibility in the Bi₂Sr₂CaCu₂O₈ system *Physica C* **282–287** 843–4
- [66] Keys S A, Koizumi N and Hampshire D P 2002 The strain and temperature scaling law for the critical current density of a jelly-roll Nb₃Al strand in high magnetic fields *Supercond. Sci. Technol.* **15** 991–1010
- [67] Taylor D M J and Hampshire D P 2005 The scaling law for the strain dependence of the critical current density in Nb₃Sn superconducting wires *Supercond. Sci. Technol.* **18** S241–52
- [68] Dew-Hughes D 1974 Flux pinning mechanisms in type II superconductors *Phil. Mag.* **30** 293–305
- [69] Kumakura H et al 1986 Synthesis of Nb₃Ga and Nb₃Al superconducting composites by laser-beam irradiation *Appl. Phys. Lett.* **48** 601–3
- [70] Kumakura H, Togano K, Tachikawa K, Tsukamoto S and Irie H 1986 Fabrication of Nb₃Al and Nb₃(Al,Ge) superconducting composite tapes by electron-beam irradiation *Appl. Phys. Lett.* **49** 46–8
- [71] Bugoslavsky Y et al 2001 Enhancement of the high-magnetic-field critical current density of superconducting MgB₂ by proton irradiation *Nature* **411** 561–2
- [72] Bauer H, Saur E J and Schmeitzer D G 1975 Effect of neutron irradiations on superconducting properties of A-15 compounds undoped and doped with ¹⁰B and ²³⁵U *J. Low Temp.* **19** 171
- [73] Nishimura A et al 2009 Neutron irradiation effects on superconducting wires and insulating materials *Fusion Eng. Des.* **84** 1425–8
- [74] Mezzetti E, Minetti B, Andreone D, Cherubini R, Gherardi L and Metra P 1992 Critical currents and dissipative effects in proton-irradiated ceramic YBCO and BISCO *J. Supercond.* **5** 185–9
- [75] Fuchs G et al 2007 Strongly enhanced irreversibility fields and Bose-glass behaviour in bulk YBCO with discontinuous columnar irradiation defects *Supercond. Sci. Technol.* **20** S197
- [76] Behera D, Patnaik K and Mishra N C 2001 Irradiation-induced inter- and intra-granular modifications by 120 MeV S Ions in YBa₂Cu₃O₇ thick films *Mod. Phys. Lett. B* **15** 69–80
- [77] Esterer M, Fugger R, Chudy M, Hengstberger F and Weber H W 2010 Neutron irradiation of coated conductors *Supercond. Sci. Technol.* **23** 014009
- [78] Wu J Z et al 1991 Anisotropic properties of the high-quality epitaxial YBa₂Cu₃O_{7-d} (110) thin film *Phys. Rev. B* **44** 12643–6
- [79] Tarantini C et al 2014 Development of very high J_c in Ba(Fe_{1-x}Co_x)₂As₂ thin films grown on CaF₂ *Sci. Rep.* **4** 7305
- [80] Dinner R B, Robinson A P, Wimbush S C, MacManus-Driscoll J L and Blamire M G 2011 Depairing critical current achieved in superconducting thin films with through-thickness arrays of artificial pinning centers *Supercond. Sci. Technol.* **24** 055017
- [81] Li G Z et al 2013 Effects of carbon concentration and filament number on advanced internal Mg infiltration-processed MgB₂ strands *Supercond. Sci. Technol.* **26** 095007
- [82] Lu X F, Pragnell S and Hampshire D P 2007 Small reversible axial-strain window for critical current in both compression and tension for a high performance Nb₃Sn superconducting strand *Appl. Phys. Lett.* **91** 132512
- [83] Hampshire D P, Jones H and Mitchell E W J 1985 An in-depth characterisation of (NbTa)₃Sn filamentary superconductor *IEEE Trans. Magn.* **21** 289–92

- [84] Mitra S, Cho J H, Lee W C, Johnston D C and Kogan V G 1989 Magnetic field penetration depth of polycrystalline (Y,Gd) $\text{Ba}_2\text{Cu}_3\text{O}_7$, grain-aligned $\text{YBa}_2\text{Cu}_3\text{O}_7$, and single crystal $\text{Bi}_2\text{Sr}_2\text{Ca}\text{Cu}_2\text{O}_8$ *Phys. Rev. B* **40** 2674–7
- [85] Li Q, Suenaga M, Gohng J, Finnemore D K, Hikata T and Sato K 1992 Reversible magnetic properties of *c*-axis-oriented superconducting $\text{Bi}_2\text{Sr}_2\text{Ca}_2\text{Cu}_3\text{O}_{10}$ *Phys. Rev. B* **46** 3195–8
- [86] Miu L, Wagner P, Frey U, Hadish A, Miu D and Adrian H 1995 Vortex unbinding and layer decoupling in epitaxial $\text{Bi}_2\text{Sr}_2\text{Ca}_2\text{Cu}_3\text{O}_{10+\delta}$ films, *Phys. Rev. B* **52** 4553–8
- [87] Junod A, Erb A and Renner C 1999 Specific heat of high temperature superconductors in high fields at T_c : from BCS to the Bose–Einstein condensation *Physica C* **317–318** 333–44
- [88] Seidel P, Grajar M, Plecenik A and Hlubina R 1996 Superconducting parameters of YBCO and BSCCO from ‘tunneling’ spectroscopy *Physica B* **218** 224–7
- [89] Okazaki N *et al* 1990 Specific-heat anomaly near T_c of the (Bi, Pb)–Sr–Ca–Cu–O superconductor $T_c = 107$ K *Phys. Rev. B* **41** 4296–301
- [90] Narsinga Rao G, Molinie P, Ganne M and Babu D S 1995 Magnetic relaxation, lower critical field and irreversibility line of W-doped (Bi, Pb)-2223 superconductor *Mod. Phys. Lett. B* **09** 1387–96